Q. J. R. Meteorol. Soc. (1997), **123**, pp. 2009–2040

Tropospheric water-vapour and ozone cross-sections in a zonal plane over the central equatorial Pacific Ocean

By D. KLEY[1]*, H. G. J. SMIT[1], H. VÖMEL[2], H. GRASSL[3], V. RAMANATHAN[4], P. J. CRUTZEN[4,5], S. WILLIAMS[6], J. MEYWERK[3] and S. J. OLTMANS[7]

[1]*Institut für Chemie und Dynamik der Geosphäre, Germany*
[2]*University of Colorado, USA*
[3]*Max-Planck-Institut für Meteorologie, Germany*
[4]*Scripps Institution of Oceanography, USA*
[5]*Max-Planck-Institut für Chemie, Germany*
[6]*University Cooperation for Atmospheric Research, USA*
[7]*NOAA Climate Modelling and Diagnostics Laboratory, USA*

(Received 7 November 1995; revised 19 October 1996)

SUMMARY

Tropospheric water-vapour and ozone measurements, using calibrated balloon-borne sensors, are reported from the Central Equatorial Pacific Experiment (CEPEX). The sensors were launched from the Research Vessel *Vickers* along 2°S latitude between 156°E (west of the international date line) and 155°W (east of the date line). These measurements are combined with those from water-vapour sondes launched over the western Pacific warm pool, during the Coupled Ocean–Atmosphere Response Experiment (TOGA–COARE). Taking the two experiments CEPEX and TOGA–COARE together, the sensors included frost-point hygrometers, Humicap-A Väisälä sondes, Humicap-H Väisälä sondes and electrochemical ozone-sondes. Taken together, the CEPEX and TOGA–COARE data provide over 150 vertical profiles of water vapour within the troposphere in varied conditions of convective activity ranging from disturbed to suppressed. The primary motivation behind the present analyses is to understand the role of tropical deep convection in the vertical distribution of water-vapour. With this in mind, the profiles have been analysed in relation to occasions of recent deep convection and occasions when convection was suppressed.

We employ three different criteria to identify the profiles influenced by deep convection: brightness temperature in the infrared-window channel of the Japanese Geostationary Meteorological Satellite (GMS); ozone as a quasi-conservative tracer for deep convection; and using water vapour itself, that is the wettest versus the driest soundings. Irrespective of the criteria used, we report here that the atmosphere, while under the influence of active deep convection, was found to have relative humidities in excess of 75% over most of the troposphere between the surface and about 14 km. The sondes were launched routinely over a period of 45 days (between CEPEX and TOGA–COARE), without biasing the sample towards convectively disturbed conditions.

A feature of the convectively disturbed profile is a distinct minimum in relative humidity at about 700 hPa, where it was as low as 65%. The low relative humidity was accompanied by relatively high ozone mixing ratios, which raises the possibility of long-range transport of dry sub-tropical air into the warm, convectively disturbed, regions of the equatorial Pacific Ocean. Inspection of the analysed fields, and the wind fields from the sondes, supports this assertion.

It then follows that the omnipresent minimum of moist static energy and minimum relative humidity at 700 hPa in the inner tropics may be the result of long-range, inclined, transport of dry air from non-convective regions. This detection suggests a linkage between the large-scale circulation, deep convection and the thermodynamic structure within the equatorial troposphere.

The results presented here demonstrate the applicability of ozone as a quasi-conservative tracer of transport in the context of deep convection.

The ozone-based criterion is used to diagnose recent deep convection, independent of the GMS satellite observations, and allows one to follow the evolution of relative humidity and of water-vapour mixing ratio after the dissipation of the cloud anvil to optically thin conditions. We show that the troposphere dries to low humidity soon after anvil dissipation. This observation leads to the hypothesis that moistening of the atmosphere, away from the core of Cb convection, occurs by evaporation of precipitation falling out of the anvils. After anvil dissipation, the ensuing subsidence in clear air causes the relative humidity and the water mixing ratio to decrease.

KEYWORDS: Balloon-borne sensors Humidity Tracer transport Tropical convection

1. INTRODUCTION

Water vapour is the most important greenhouse gas. About 90% of the atmospheric greenhouse effect results from the presence of water in the form of vapour and clouds. The balance is caused by CO_2, O_3 and numerous other trace gases. Water vapour also

* Corresponding author: Institut für Chemie und Dynamik der Geosphäre, Forschungszentrum Jülich, 52425 Jülich, Germany.

plays a significant role in the atmospheric general circulation. Accumulated by the lower trade-winds, latent heat is carried to the equatorial-trough zone where it is used for lifting and conversion of energy, balancing radiative losses, and to export the residual polewards in the form of sensible heat and potential energy.

Deep convection was identified by Riehl and Malkus (1958) as the mechanism by which energy and mass is directly transported from the boundary layer to the upper tropical troposphere. The transport is achieved in undiluted hot towers of cumulonimbus convection, bypassing the middle troposphere. As a result of these intermittent processes, the profile of moist static energy in the equatorial-trough zone has a minimum near 700 hPa so that, thermodynamically, energy transport to that level occurs both from below and from above, along the energy gradient. It is clear, however, that a static picture, such as a two-dimensional (2-D) field of moist static energy does not provide evidence for the processes by which it is generated and maintained.

Key to the understanding of deep convection is the measurement of water vapour and total water (vapour plus condensed) on time- and space-scales at which the process occurs. This is a difficult task because:

- aircraft are seldom, if ever, directed close to the undiluted hot towers of deep convection;
- radiosonde balloons, carrying meteorological instrumentation, are frequently destroyed in the harsh environment of tropical thunderstorms or are expelled from the core environment;
- satellite instruments cannot look through the frequent uppermost cirrus decks;
- the accuracy and precision of standard meteorological humidity sensors are not well known.

It has been debated whether deep convection moistens or dries the upper tropical troposphere. Sun and Lindzen (1993) examined the observed distribution of tropical tropospheric water-vapour using conventional radiosonde data and satellite-derived humidities in the context of a heuristic model of tropical convection. They noted that the tropical troposphere is subsaturated, both with respect to liquid water and ice, and that the relative humidity with respect to ice in the upper troposphere is low and does not drop much on the way to the lower troposphere. According to Sun and Lindzen, these observations imply the presence of a convectively driven macroscale circulation which prevents the atmosphere from attaining saturation and which involves the evaporation of hydrometeors in the subsiding air.

In our view, the data employed by Sun and Lindzen suffer from a dry bias. Satellite observations cannot probe below cloud decks and, therefore, favour areas of subsidence. The rawinsonde data show relative humidities with respect to ice, and averaged over the domain of the Hadley-cell circulation, of only 40% between 600 hPa and 300 hPa, above which the humidity sensors used operationally become unreliable. Even 40% seems to be large according to Sun and Lindzen: in their model, evaporating hydrometeors are the source of water vapour to the subsiding air.

Several kinds of humidity sensors are used for research purposes. Foremost is the NOAA frost-point hygrometer. It has been used to obtain trends of stratospheric water-vapour above Washington, D.C. (Mastenbrook 1968) and Boulder, Colorado (Mastenbrook and Oltmans 1983); specifically designed to measure stratospheric water-vapour, it operates below 0 °C and, by virtue of its simple thermodynamic working principle, also provides accurate humidity-profiles in the troposphere. The frost-point hygrometer has provided the in-flight calibrations for most of the recent satellite water-vapour instruments. Another instrument, the Lyman alpha fluorescence hygrometer, designed by Kley and Stone (1978),

measures the water-vapour mixing ratio and has been used at heights above 600 hPa. Intercomparison between the balloon-borne frost-point hygrometer and the Ly(α) fluorescence hygrometer in the laboratory gave agreement at the 3% level (Kelly, personal communication). Field intercomparisons between these instruments give, however, worse agreement ($\sim$18%) (Burnett *et al.* 1985; Vömel H. *et al.*, personal communication). The source of the disagreement is not clear. However, there is no doubt that either one of the two instruments is the device of choice to perform high quality ascents in the upper troposphere and in the stratosphere.

Unfortunately, these instruments are expensive. In particular, the Ly(α) device is too expensive to be operationally expendable. The frost-point hygrometer, although not cheap, can be used as a reference instrument on campaigns, either alone or to test less accurate devices. This has been done in the present study, where the frost-point hygrometer provided occasional accurate profiles against which to check and calibrate thin-film capacitative humidity sensors (Humicap). (They are in wide operational use by national meteorological services in Europe.)

Field intercomparisons of the thin-film humidity sensor against accurate reference instruments, such as the frost-point hygrometer, have not been reported. Therefore, before far-reaching, and possibly wrong, conclusions about the effects of deep convection on the water-vapour distribution in the upper troposphere are drawn, it is essential to obtain precise and accurate measurements of water vapour.

In the present paper, we report water-vapour measurements over the tropical equatorial Pacific Ocean obtained with thin-film capacitive sensors (Humicap) and with carbon hygristors. Reference profiles from frost-point hygrometers are used to validate the data obtained with the thin-film sensors.

The scientific objectives of the water-vapour measurements were, firstly, to measure the west–east gradient of tropical water-vapour and its vertical distribution with high spatial and temporal resolution, and, secondly, to determine how deep convection affects density and vertical distribution of water vapour in the tropical trough-line region. While the achievement of the first objective presents a technical challenge, the attainment of the second is difficult in a more general sense. The use of water in any of its three phases to elucidate the role of deep convection on the spatial and temporal distribution of atmospheric water makes water an independent and, simultaneously, a dependent variable. It would be advantageous if a non-water tracer for the diagnosis and the details of deep convection could be identified, so that the measurement of the water substance would represent a truly dependent variable.

In the present paper, we take tropospheric ozone as an additional tracer for the extent and intensity of deep convection over the central Pacific Ocean. Consideration of the photochemical lifetime of ozone over the tropical ocean as a function of altitude shows that ozone may indeed be treated as a quasi-conservative tracer in the free troposphere. Boundary-layer ozone over the equatorial Pacific has a photochemical lifetime of approximately five days because of photochemical destruction involving water vapour and solar ultraviolet radiation (Crutzen 1973; Liu *et al.* 1983):

$$\begin{array}{lll} \text{R1} & O_3 + h\nu(\lambda < 325\ \text{nm}) & \longrightarrow \quad O(^1D) + O_2 \\ \text{R2} & O(^1D) + H_2O & \longrightarrow \quad 2OH \\ \hline \text{net C1:} & O_3 + H_2O & \longrightarrow \quad 2OH + O_2. \end{array}$$

In addition, in NO_x-poor environments such as the atmosphere over the Pacific (because of the lack of significant NO sources (McFarland *et al.* 1979; Torres and Thompson 1993)), ozone is also lost by the reactions

$$\begin{array}{lll} \text{R3} & \text{CO} + \text{OH} + \text{O}_2 & \longrightarrow \quad \text{HO}_2 + \text{CO}_2 \\ \text{R4} & \text{HO}_2 + \text{O}_3 & \longrightarrow \quad \text{OH} + 2\text{O}_2 \\ \hline \text{net C2:} & \text{CO} + \text{O}_3 & \longrightarrow \quad \text{CO}_2 + \text{O}_2. \end{array}$$

In the free troposphere, because of the lower absolute concentration of water vapour and the corresponding decrease of the O_3 destruction rate by reactions R1–R4, the lifetime of ozone against photochemical destruction is much longer than in the boundary layer. Once an ozone molecule has left the subcloud layer in a forced Cb ascent and has reached an altitude above 9 km, its lifetime is estimated to be 40 days. Near the tropopause, the ozone lifetime increases to about a year.

So, the lowest troposphere over the equatorial Pacific Ocean is a chemical ozone-sink. Indeed, numerous measurements of low ozone-concentrations have been reported in the marine boundary layer (Liu *et al.* 1983; Piotrowicz *et al.* 1986, 1991; Johnson *et al.* 1990; Thompson *et al.* 1993).

Cumulonimbus convection lifts subcloud-layer air and transports it to the upper troposphere above 10 km in a forced ascent. Since the ozone concentrations at these heights are generally well above those that are known to exist in near-surface air of the equatorial Pacific, active or recent deep convection should be identifiable by low ozone-concentrations in the upper troposphere. These considerations provided the motivation to measure ozone simultaneously with the water-vapour concentration.

2. Experimental details

(*a*) *Central Equatorial Pacific Experiment (CEPEX)*

CEPEX was conducted from 7 March 1993 to 7 April 1993. The objectives and experimental design are described in detail in the CEPEX experimental design document (CEPEX 1993). One of the major objectives of CEPEX was to measure the east–west cross-section of the vertical water-vapour distribution from the sea surface to about 25 km, along the equatorial Pacific. The CEPEX platforms included aircraft flights along the 2°S latitude line, about 15° west and east of the international date line, i.e. 165°E (E is west of the date line) to 165°W (W is east of the date line). It also included the research vessel R/V *Vickers*, cruising along the 2°S latitude line, in the CEPEX domain of 160°E to 160°W. The *Vickers* had been participating in the TOGA–COARE experiment (Webster and Lukas 1993), which was conducted over the western Pacific warm pool between November 1992 and February 1993.

The data used in the present study consist of the following balloon-borne data taken during CEPEX:

(i) Humicap A Väisälä sondes 31
(ii) electrochemical concentration cells (ECC) ozone-sondes 31
(iii) frost-point hygrometer with ECC ozone-sondes 13
(iv) Humicap H series Väisälä sondes, launched by the Max-Planck-Institut für Meteorologie, Hamburg, referenced as MPI series 47

In addition to the humidity measurements made by these 'upsondes', we have used 'dropsondes' (VIZ) that were deployed from a high-flying aircraft:

(v) VIZ dropsondes 50

We also combine these with the sondes launched from the *Vickers* during the TOGA–COARE experiment, over the warm pool

(vi) Humicap H launched during TOGA–COARE, by MPI 118.

(*b*) *Water-vapour instrumentation*

The frost-point hygrometer (FPH) is a balloon-borne device, originally developed by Mastenbrook (1966, 1968), and modified by Mastenbrook and Oltmans (1983) which has been used on many occasions in the stratosphere. The FPH measures the temperature of a chilled mirror at which a frost layer forms (Vömel *et al.* 1995a). Although not optimized for tropospheric applications it is considered accurate to within ± 1 °C of the frost point. The stated accuracy of this instrument is mainly determined by its precision, which is also ± 1 °C of the frost point. From comparisons of frost-point-derived humidities in the stratosphere above 20 km with relevant data from the HALOE instrument on the Upper Atmosphere Research Satellite (UARS), it was discovered (Vömel *et al.* 1995b) that some of the CEPEX soundings suffered from a radio-frequency interference problem. In those cases, the interference created an error in the value of the frost point which was independent of altitude. Vömel *et al.* (1995b) have used results from the HALOE experiment on the UARS as reference values at one stratospheric altitude. The radio-frequency interference caused a precision error of approximately ~ 1.5 °C in the frost point. In the upper troposphere, the correction procedure produces slightly higher relative humidities over ice ($\sim 10\%$), as compared to the uncorrected profiles. For CEPEX, we took a conservative approach, by applying no correction and by degrading the total uncertainty of the FPH soundings to ± 2 °C. The uncertainty of the FPH at -73 °C, corresponding to an altitude of 15 km, is then $+25/-30\%$ of relative humidity over ice. In the middle troposphere, at 6 km, the uncertainty is $+16/-18\%$.

The ambient (dry) temperature of the frost-point hygrometer package is measured by an attached RS-80 radiosonde (Thermocap). Radiative corrections to the radiosonde-derived air temperature, arising from insolation effects to the temperature sensor, are corrected by following the instructions from the manufacturer. The frost-point hygrometers, together with radiosonde and electrochemical ozone sensors, were launched on small valved rubber balloons. Data were recorded and used from balloon ascent and descent.

The Humicap A (Väisälä 1991) is a thin-film polymer capacitive sensor whose capacity depends on the amount of water absorbed by the polymer. The Humicap A is used in many operational radiosonde networks throughout the world, especially in Europe, where it is an integral part of the RS-80 radiosonde. The sonde was deployed, together with the ECC ozone-sonde, either on 600 g rubber balloons (VO package) or, together with ECC and frost-point hygrometer, on 2000 g rubber balloons (VOF package). The Humicap A is normally used with a small aluminized cap over the humidity-sensing capacitor to protect it from direct rain and radiation effects. However, in order to increase ventilation and thus to decrease a possible sensor time lag of the ascending package relative to the local environment, it was decided to fly the VO and the VOF sondes without the cap over the thin-film humidity sensors. Irrespective of whether a cap is employed to protect the sensor or an unprotected sensor is used, icing can occur if supercooled droplets hit the sensor or its surroundings (Antikainen and Paukkunen 1994). Once an ice layer has formed, it usually takes a considerable time to evaporate, rendering the humidity measurement of the ascending package of little use. Individual soundings must be carefully studied for this effect. Icing is clearly indicated when high relative humidity is reported above the tropopause. In summary, the VO package measured relative humidity, ozone, dry temperature and pressure. The VOF package measured frost point, relative humidity, ozone, dry temperature and pressure.

A newer version of the humidity sensor on the RS-80 radiosonde became available recently. This Humicap-H sensor employs a different thin-film material and is smaller than the Humicap A (Antikainen and Paukkunen 1994). As well as the VO/VOF series,

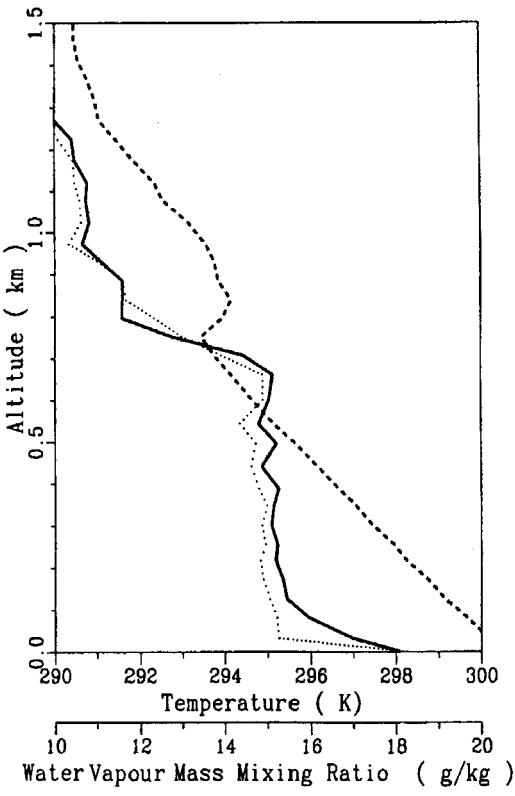

Figure 1. MPI sounding number 34: temperature (K) (dashed); water vapour mixing ratio (g kg^{-1}) without corrections (dotted); water vapour mixing ratio (g kg^{-1}) with corrections (solid).

another radiosonde operation (MPI series) was performed with the Humicap-H sensor on the RS-80 sonde. Just before the sonde was released, a thorough check was made of temperature, pressure and humidity against a shipboard meteorological station on the stern deck. This procedure enabled the application of an initial temperature correction, outlined in the following paragraph.

The procedure for obtaining pressure, temperature and humidity information from the radiosonde signal has been outlined in the information bulletin SR 0559 (Väisälä 1991). Cole (1993a) developed a correction procedure that was followed for the MPI series. In short, because of high solar insolation, and lack of ventilation prior to release of the sonde, sensors can be up to 5 °C higher than ambient temperature which, in the absence of proper ventilation, can result in relative humidities up to 20% too low. After sonde release, and the beginning of ventilation, the temperatures of the substrates of the humidity sensor and the temperature sensor adjust to ambient conditions. If true values of surface temperature and relative humidity are known, as they were from the meteorological station, then, it is possible to generate correction factors for every data frame that the sonde transmits.

The results of the correction procedure can be summarized as follows: near ground, the specific humidity is about 2–3 g kg^{-1} larger than that determined without correction. This correction factor (~10%) decays to zero at 950–900 hPa. In the mean, the total water column density of the atmosphere is increased by 1.3–1.5 kg m^{-2}. Figure 1, as an example, shows the effects of correction on MPI sounding 34. An increase in specific humidity of roughly 10% is apparent near the surface.

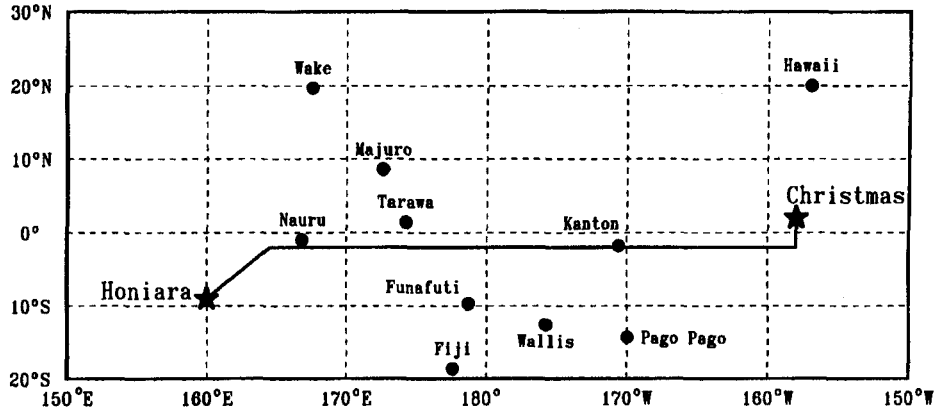

Figure 2. Cruise track of the R/V *Vickers* between Honiara (Solomon Islands) and Christmas Island during CEPEX.

In addition to the humidity measurements made by the various types of upsondes, we have also deployed dropsondes from a high flying Lear Jet aircraft. The dropsondes used heated carbon hygristors made by VIZ as modified by Cole (1993b).

(*c*) *Ozone instrumentation*

Ozone partial pressures were measured with electrochemical concentration cells (ECC). The ECCs were part of the VO and VOF sounding packages. Extremely low ozone-concentrations were measured during the expedition which necessitated a post-experimental determination of the ECC accuracy under the specific conditions encountered (Smit *et al.* 1994). The uncertainty of the determination of the ozone partial pressure was 0.1 mPa, found employing a data-reduction procedure where the correction for the background current subtraction of the ECC was independent of the O_2 partial pressure. In terms of volume mixing ratio, the uncertainty was ± 1–2 parts in 10^9 (p.p.b.v.) below 5 km, increasing to ± 5 p.p.b.v. at 13 km altitude.

(*d*) *The cruise of the R/V* Vickers *and the flights of the Lear Jet*

The radiosondes (upsondes) were launched from a ship. During February 1993 the R/V *Vickers* was stationed at 156°E, 2°S in the context of the Tropical Ocean Global Atmosphere–Coupled Ocean–Atmosphere Response Experiment (TOGA–COARE). A total of 118 successful upsondes (MPI series) were launched while the *Vickers* was on station. The *Vickers* then sailed to Honiara, Solomon Islands (160°E, 9°30′S). It left port on 7 March 1993 to make various measurements in the context of the Central Equatorial Pacific Experiment (CEPEX 1993), arriving at Christmas Island (157°12′W, 1°30′N) on 18 March. The MPI equipment stayed on board and also operated after the vessel left Christmas Island on 19 March. The VO and VOF equipment was operated only during the CEPEX cruise from Honiara to Christmas Island, where it was unloaded. It continued to operate on the island. The *Vickers*, after steaming north-east from Honiara for approximately three days, cruised due east at 2°S latitude until 17 March. It then changed course on the way to Christmas Island (Fig. 2). Table 1 contains a compilation of sonde launches of the VO and VOF type and Table 2 lists the CEPEX–MPI series of radiosondes. All launch times are given as Greenwich Mean Time (GMT).

TABLE 1. DATES AND LOCATIONS OF BALLOON SOUNDINGS FROM R/V *Vickers* (VO, VOF SERIES)

Flight	Date	Time (GMT)	Location	Ceiling (km)	Instruments	
1	7 March	0932	9°25′S, 159°58′E	17.0	FPH, O_3, rel. hum.	VOF
3	9 March	2259	2°07′S, 169°35′E	31.6	O_3	VO
6	11 March	0657	2°07′S, 175°20′E	31.8	O_3	VO
8	12 March	0503	2°00′S, 178°46′E	26.3	FPH, O_3, rel. hum.	VOF
9	12 March	0933	2°00′S, 179°30′E	31.0	O_3	VO
10	13 March	0130	2°00′S, 178°02′W	30.1	FPH, O_3, rel. hum.	VOF
11	13 March	0811	2°00′S, 176°57′W	32.3	O_3	VO
12	13 March	2329	2°00′S, 174°46′W	23.5	FPH, O_3, rel. hum.	VOF
13	14 March	0807	1°59′S, 173°39′W	32.2	O_3	VO
14	14 March	2159	1°59′S, 171°23′W	29.1	FPH, O_3, rel. hum.	VOF
15	15 March	0754	1°59′S, 169°43′W	27.8	O_3	VO
16	15 March	2221	1°59′S, 167°07′W	29.5	FPH, O_3, rel. hum.	VOF
18	16 March	2043	1°59′S, 162°55′W	32.4	FPH, O_3, rel. hum.	VOF
19	17 March	0704	2°00′S, 161°11′W	29.5	O_3	VO
20	17 March	2127	1°04′S, 159°03′W	28.1	FPH, O_3, rel. hum.	VOF
21	18 March	0658	0°16′N, 158°25′W	31.4	O_3	VO
22	20 March	0808	1°30′N, 157°12′W	32.4	FPH, O_3, rel. hum.	VOF
23	21 March	0058	1°30′N, 157°12′W	31.0	O_3	VO
24	22 March	0100	1°30′N, 157°12′W	31.0	O_3	VO
25	22 March	2138	1°30′N, 157°12′W	26.9	FPH, O_3, rel. hum.	VOF
26	23 March	0408	1°30′N, 157°12′W	33.3	O_3	VO
27	24 March	0000	1°30′N, 157°12′W	26.4	FPH, O_3, rel. hum.	VOF
28	24 March	0819	1°30′N, 157°12′W	33.1	O_3	VO
29	24 March	2212	1°30′N, 157°12′W	26.8	FPH, O_3, rel. hum.	VOF
30	25 March	0758	1°30′N, 157°12′W	33.9	O_3	VO
31	26 March	0118	1°30′N, 157°12′W	27.1	FPH, rel. hum.	VOF
32	26 March	0444	1°30′N, 157°12′W	32.2	O_3	VO

FPH indicates frost-point hygrometer; O_3 refers to ECC and rel. hum. stands for Väisälä Humicap-A sensor.

The dropsondes were deployed from a Lear Jet aircraft which flew at altitudes varying from 8 to 15 km. Suppressed, layer cloud, and convective conditions were sampled. In cloudy conditions, most of the sondes were released from 8 km, whereas in clear conditions they were mostly released from about 13 km. Data from the first 100 hPa of each descent, during which the instruments adjusted to equilibrium, have been discarded. A total of 17 missions was flown, deploying 98 dropsondes successfully (defined here as providing data at least down to 900 hPa). The majority of these were deployed at 2°S between 165°E and 170°W, with the remainder south of this segment as far as 18°S. The missions were staggered through the experiment, from 8 March to 6 April 1993. For details of the flight plans and weather conditions see the CEPEX Operations Summary (Williams 1993).

3. VALIDATION OF UPSONDES

In this section, the performance of the radiosonde-derived humidities, as obtained from the shipboard releases, is compared with those from the frost-point hygrometer (FPH). Two independent methods of comparison were used: firstly, Humicap A against frost-point-hygrometer-derived humidity (abbreviated to VO against FPH); secondly, Humicap H against frost-point-hygrometer-derived humidity (MPI against FPH). For this comparison, proper selection from many MPI soundings needed to be made to get the best coincidence in time with the independently flown frost-point hygrometers.

TABLE 2. DATES AND LOCATIONS OF MPI BALLOON SOUNDINGS FROM R/V *Vickers*

MPI Flight	Day in March	Time (GMT)	Location
1	4	0338	9°25′S, 159°58′E
2	7	1807	7°57′S, 160°43′E
3	8	0005	6°50′S, 161°24′E
4	8	0540	5°51′S, 162°01′E
5	8	1153	4°40′S, 162°40′E
6	8	1757	3°42′S, 163°21′E
7	9	0001	3°22′S, 164°39′E
8	9	0556	3°04′S, 165°50′E
9	9	1206	2°10′S, 167°14′E
10	9	1757	2°24′S, 168°25′E
11	9	2358	2°03′S, 169°41′E
12	10	0557	1°59′S, 170°47′E
13	10	1201	2°00′S, 172°02′E
14	10	1845	1°59′S, 173°21′E
15	11	0003	1°58′S, 174°09′E
16	11	0602	2°07′S, 175°19′E
17	11	1200	2°04′S, 176°18′E
18	11	1801	2°00′S, 177°24′E
19	12	0002	1°58′S, 178°28′E
20	12	0603	1°59′S, 178°58′E
21	12	1202	2°00′S, 179°51′E
22	12	1758	1°58′S, 179°14′W
23	13	0006	2°00′S, 178°04′W
24	13	0558	1°58′S, 177°17′W
25	13	1205	1°58′S, 176°30′W
26	13	1755	2°00′S, 175°30′W
27	13	2353	1°58′S, 174°46′W
28	14	0558	2°00′S, 174°01′W
29	14	1157	2°00′S, 173°01′W
30	14	1802	2°00′S, 171°53′W
31	14	2357	2°00′S, 171°04′W
32	15	0606	2°00′S, 170°30′W
33	15	1158	2°00′S, 169°02′W
34	15	1800	1°58′S, 167°53′W
35	15	2357	1°58′S, 166°56′W
36	16	0558	1°58′S, 165°45′W
37	16	1159	2°00′S, 164°45′W
38	16	1756	1°58′S, 163°33′W
39	16	2355	1°58′S, 162°30′W
40	17	0553	1°58′S, 161°22′W
41	17	1152	2°00′S, 160°18′W
42	17	1802	1°40′S, 159°19′W
43	17	2353	0°47′S, 158°54′W
44	18	0555	0°08′S, 158°29′W
45	18	1156	1°10′N, 158°01′W
46	18	1756	1°59′N, 157°29′W
47	19	0556	2°03′N, 157°11′W

The humidity sensors were of the Väisälä Humicap-H type.

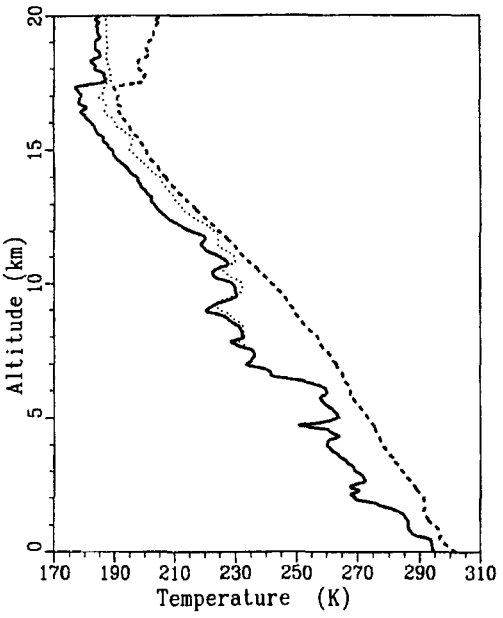

Figure 3. VOF flight number 16: dry temperature (K) (dashed); frost point (K) from the frost-point hygrometer (dotted); frost point (K) from the Humicap-A sensor (solid).

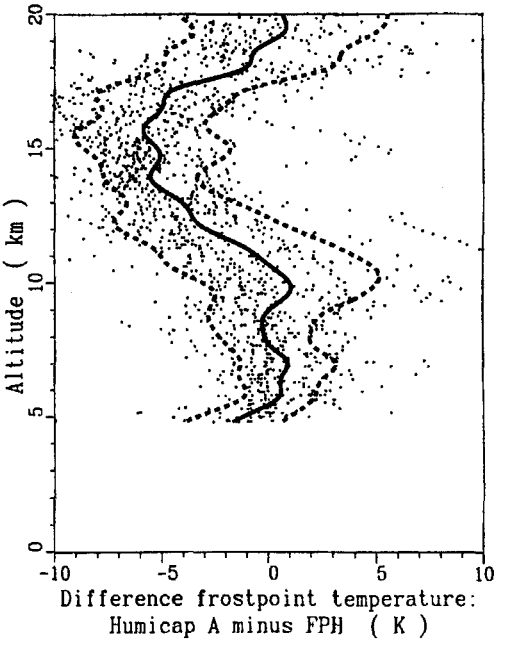

Figure 4. Differences (K) of Humicap-A-derived frost-points from frost points measured by the frost-point hygrometer: mean (solid); $\pm 1\sigma$ standard deviation (dashed). The data points are averages over intervals of 250 m of height. Data were used from all the R/V *Vickers* soundings plus soundings over Christmas Island.

(*a*) *VO versus FPH*

Temperature (T), frost-point-hygrometer-derived frost-points (FPH) and Humicap-A-derived frost-points from VOF flight 16 are plotted as an example in Fig. 3. Since the frost-point hygrometer is not operational at temperatures above 0 °C, no FPH results are given in Fig. 3, and in other relevant figures, below the altitude of approximately 5 km. Inspection of Fig. 3 reveals excellent agreement below 10 km between the Humicap-A-derived frost-point and that from the frost-point hygrometer. Above 10 km, the Humicap A reads too dry. Differences between Humicap-A- and FPH-derived frost-points from all relevant *Vickers* soundings, plus all soundings made from Christmas Island, are shown in Fig. 4. This scatter plot reveals a small positive bias of the Humicap A at low altitudes and a trend to a negative bias of approximately 6 K at 16 km. The standard deviation about the mean is relatively constant at about ± 3 K. It contains precision and accuracy errors of both sensors. The error is only slightly larger than the accuracy error of the FPH. Since the sensors were flown on the same balloon, both were exposed to identical humidities. Consequently, Fig. 4 represents a true evaluation of the Humicap-A sensor under these conditions (no cap).

(*b*) *MPI versus FPH*

In order to make a meaningful comparison between humidities as determined by the MPI series (which used the Humicap H) and those from the frost-point hygrometers, pairs,

TABLE 3. PAIRS, OR TRIPLES, OF VOF AND MPI SOUNDINGS USED FOR ASSESSMENT OF HUMICAP-H SENSOR PERFORMANCE

VOF flight	MPI flight	Day in March	Launch time (GMT)	Location at launch
1		7	0932	0°25′S, 159°58′E
	2	7	1807	7°57′S, 160°43′E
8		12	0503	2°00′S, 178°46′E
	20	12	0603	1°59′S, 178°58′E
10		13	0130	2°00′S, 178°02′W
	23	13	0006	2°00′S, 178°04′W
12		13	2329	2°00′S, 174°46′W
	27	13	2353	1°59′S, 174°46′W
14		14	2159	1°59′S, 171°23′W
	30	14	1802	2°00′S, 171°53′W
	31	14	2357	2°00′S, 171°04′W
16		15	2221	1°59′S, 167°07′W
	34	15	1800	1°59′S, 167°53′W
	35	15	2357	1°59′S, 166°56′W
18		16	2043	1°59′S, 162°55′W
	38	16	1756	1°59′S, 163°33′W
	39	16	2355	1°59′S, 162°30′W
20		17	2127	1°04′S, 159°03′W
	43	17	2353	0°47′S, 158°54′W
22		20	0808	2°00′N, 157°30′W
	51	20	0600	1°59′N, 152°16′W

and sometimes triples, of soundings were identified which had a maximum coincidence in launch time. Selected soundings are listed in Table 3.

The statistical evaluation of all paired Humicap H–FPH soundings is shown in Fig. 5 as a scatter plot of frost-point differences (Humicap H minus FPH). Compared to the Humicap-A sensor, the Humicap H gives a better performance in the upper troposphere. The mean of the frost-point differences is very close to zero above 9 km. A small positive bias (0–2 K) is indicated below 9 km. However, the standard deviation about the mean is approximately ±3 K, so that the achieved precision was not good enough to ascertain a bias. The standard deviation in the middle troposphere is slightly wider than that of Fig. 4. This is probably caused by the natural variability of humidity between the non-collocated soundings.

A detailed comparison of sounding pairs revealed a time-constant problem of the Humicap H sensor that is not apparent from the statistical analysis. The time constant of the sensor is about 200 s at −60 °C and even longer at lower temperatures (Antikainen and Paukkunen 1994). This causes a humidity lag of the ascending package and an integration effect. At an ascent rate of 5 m s^{-1}, a time constant of 200 s causes a δ-functional humidity structure to be widened to 1 km. At a temperature of −70 °C, the time response of the sensor increases to about 400 s, corresponding to a 2 km width of a humidity spike. This integrative effect leads to a reduced amplitude of relative-humidity changes. Therefore, even if the statistical comparison of the Humicap H against the frost-point hygrometer does not reveal a bias problem, it is possible that saturation, if it occurs in narrow layers in the uppermost troposphere, will escape observation.

(c) *Assessment of humidity-sensor accuracy and precision*

The basic data for the upsonde assessment are depicted in Figs. 4 and 5. Below approximately 9 km, both configurations of the RS-80 humidity sensors worked well.

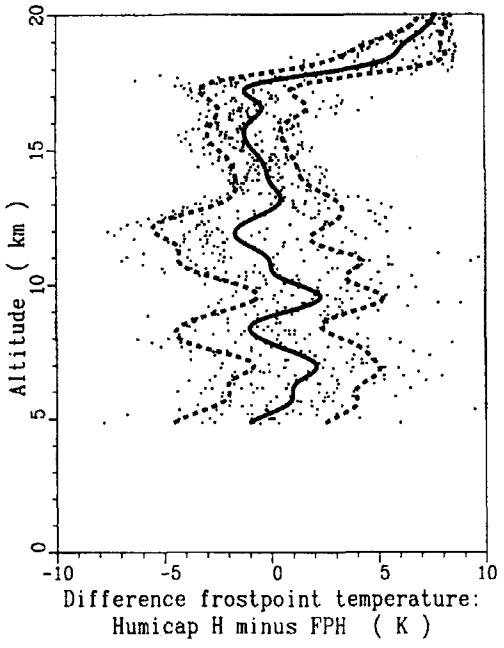

Figure 5. Differences (K) of frost points measured by MPI soundings from frost points measured by the frost-point hygrometer: mean difference (thick solid) and $\pm 1\sigma$ standard deviations (dashed). Data points are averages over intervals of 250 m of height.

Above 9 km, the Humicap-H sensors on the MPI flights worked considerably better than the Humicap-A sensors on the VO and VOF flights. The Humicap A experienced a dry bias increasing to approximately −6 K at 16 km. It is not unlikely that a revised algorithm for this sensor could be developed which would result in a more accurate data-reduction procedure. However, prior laboratory experiments are needed. In the context of CEPEX, the Humicap-A-derived humidities are clearly inferior to those obtained with the Humicap H (MPI series). Consequently, the MPI series will be used as the basis for the results and analyses.

Turning to accuracy and precision for the MPI soundings, Fig. 5 shows that, above ~9 km, there is practically no bias since the line that connects the means of the individual differences of frost point (MPI minus FPH) lies very close to zero difference. The achieved precision of the MPI humidity soundings is approximately ±2 °C of frost point above 12 km.

In the middle troposphere, below 9 km, the precision error of the MPI soundings increases to ±3 °C. A 3 °C precision error in frost point corresponds to a 10–15% relative humidity error in the middle troposphere. The precision error is slightly larger in the upper troposphere.

The total uncertainty of the MPI sounding is composed of the precision error of the Humicap-H ascents plus the ±2 K uncertainty of the FPH sensor. In the middle troposphere this corresponds to a total uncertainty for a MPI sounding of +35/–27% in relative humidity. At 15 km altitude (200 K), the uncertainty of the Humicap-H sounding is assessed at +53/−35% of relative humidity. The assessment of total uncertainty is conservative and represents upper limits, since changes of humidity are likely to have occurred in the interval between the flights of the frost-point hygrometers and the MPI radiosondes.

TABLE 4. ERROR ANALYSIS SUMMARY OF FROST-POINT HYGROMETER FOR R/V *Vickers* CRUISE

Altitude (km)	Precision[1] (K)	Accuracy[1] (K)	Uncertainty of RH (%)
> 5–16	±1.5	±2	
6			+16/−18
15			+25/−30

[1]Includes precision error due to radio interference.

TABLE 5. ERROR ANALYSIS OF VÄISÄLÄ HUMICAP-A SENSOR RELATIVE TO FROST-POINT HYGROMETER (FPH)

Altitude (km)	Bias[1] (K)	Precision (K)
0–5		
5–10	<+1	±2
10–15	+1 to −6	±3

[1]Difference of frost point (Humicap-A minus FPH).

TABLE 6. ERROR ANALYSIS OF VÄISÄLÄ HUMICAP-H SENSOR RELATIVE TO FROST-POINT HYGROMETER (FPH)

Altitude (km)	Bias (K)	Precision[1] (K)	Precision[1] (%)	Uncertainty of RH[2] (%)
0–5	not determined			
5–10	<+1[4]	±3	±(10–15)	+35/−27
11–15	0	±2	±20	+53/−35[3]

[1]Includes variability caused by non-collocation of MPI and FPH soundings.
[2]Includes uncertainty of FPH reference instrument.
[3]At 15 km (200 K ambient temperature).
[4]Not significant within precision error.

A summary of the error analyses for the humidity sensors is given in Tables 4–6. An objective assessment of accuracy and precision of the dropsonde-derived humidities against the FPH cannot be given. The limited comparison against the Väisälä upsondes and frost-point hygrometers on the Lear Jet during spiral descents has revealed a cold bias of approximately 2 K above 5 km, up to the limit of performance between 8 and 9 km. The humidity cross-sections from the dropsonde data set will be used in a relative sense to obtain information on the state of humidity in a temporal reference frame.

4. WATER-VAPOUR DISTRIBUTION

(*a*) *Profiles and cross-section of relative humidity and mixing ratio of water vapour*

Plotted in Fig. 6(a)–(h) are all individual profiles of relative humidity over ice, as measured by the frost-point hygrometers. The range of uncertainty ($\pm 1\sigma$) that results from a ±2 K error of frost point is also shown.

Figure 7 presents the cross-section of relative humidity between Honiara and Christmas Island, as obtained with the Humicap-H sensor (MPI series). (Here, and elsewhere in the present paper, relative humidities are given with respect to liquid water when $T > 273$ K

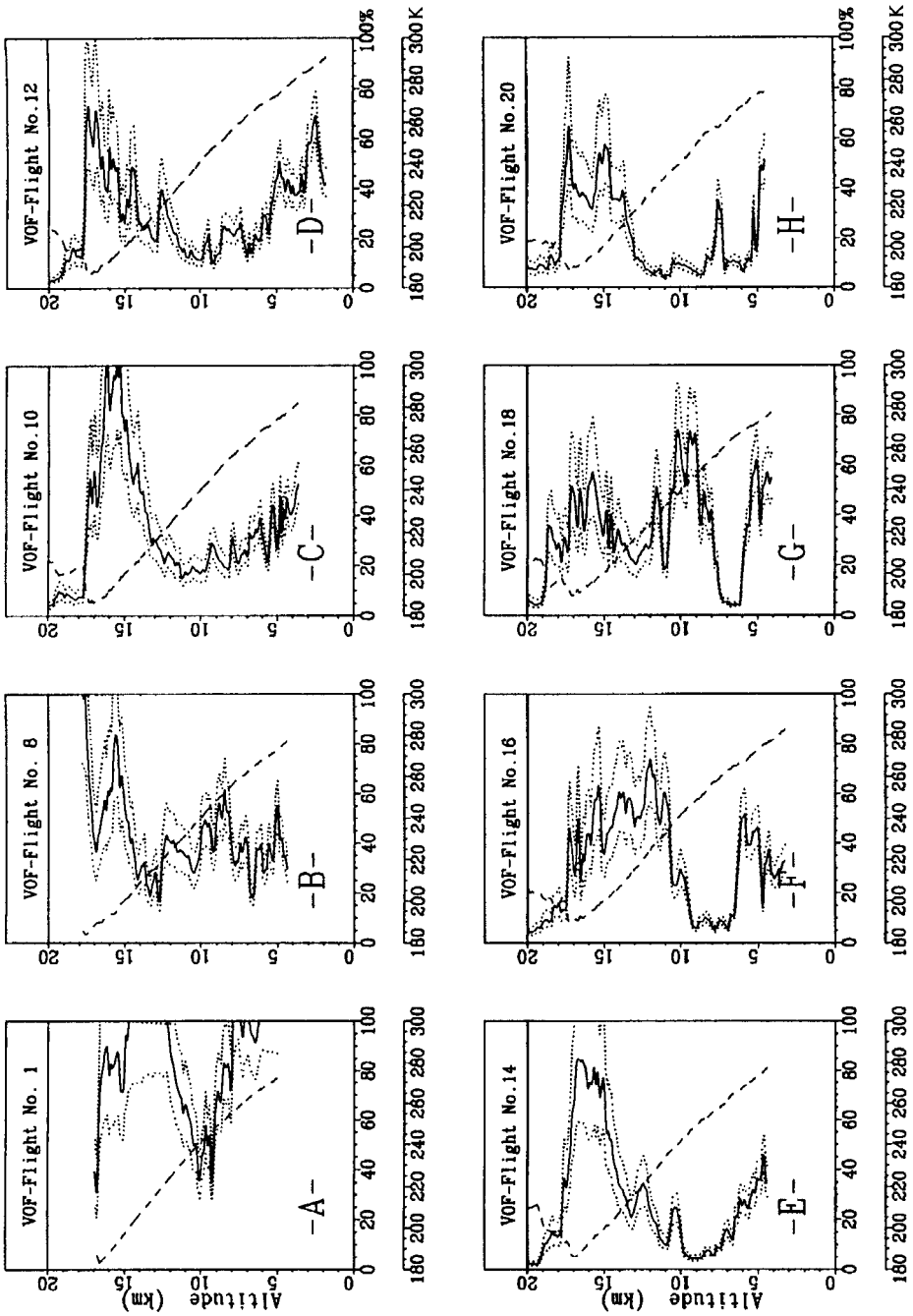

Figure 6. Profiles: relative humidity (%) from frost-point hygrometer soundings (solid); temperature (K) (dashed). Uncertainty limits (dotted) correspond to the total error of ±2K in the determination of frost points. Relative humidities are with respect to liquid water for dry temperatures above 273 K and with respect to ice below 273 K.

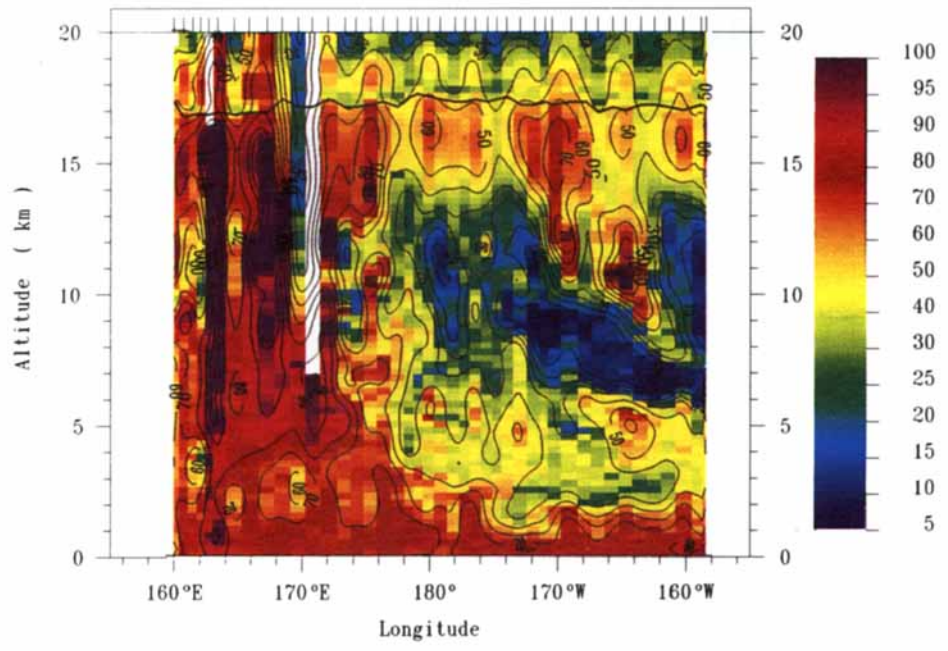

Figure 7. Two-dimensional longitude–altitude cross-section of relative humidity (%) from the R/V *Vickers* cruise along 2°S, 160°E to 160°W 7–18 March 1993. Short bars along the top of the diagram indicate longitudes of soundings. The black line indicates location of the tropopause. Relative humidities are with respect to liquid water for dry temperatures above 273 K and with respect to ice below 273 K.

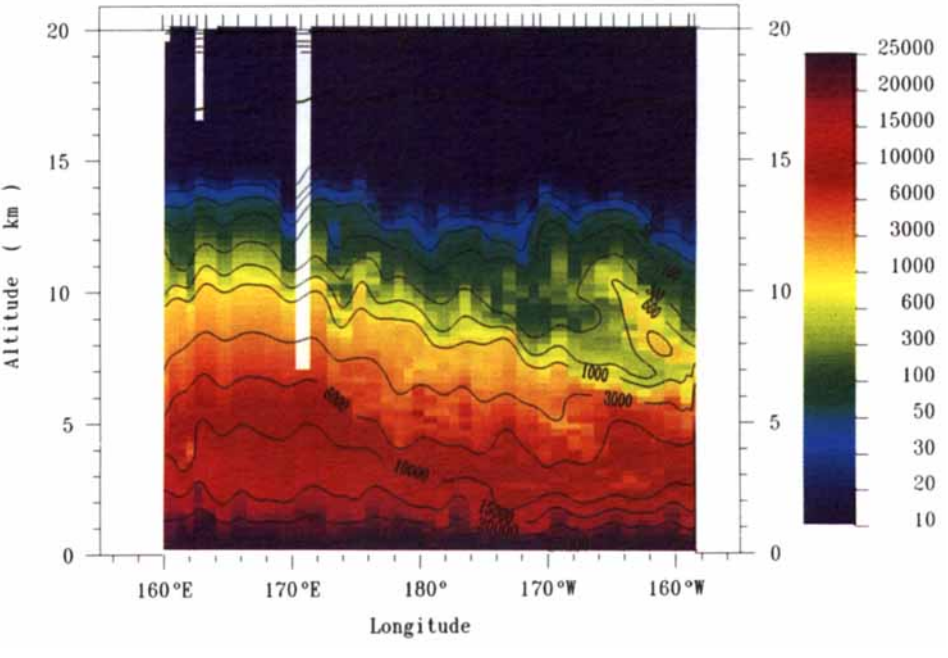

Figure 8. Two-dimensional longitude–altitude cross-section of mixing ratio of water vapour (parts per million by volume) from the R/V *Vickers* cruise along 2°S, 160°E to 160°W 7–18 March 1993, obtained from MPI soundings. Short bars along the top of the diagram indicate longitudes of soundings. The black line indicates location of the tropopause.

and with respect to ice when $T < 273$ K.) Figure 8 shows mixing ratios. Validated against the frost-point hygrometer above 5 km, Figs. 7 and 8 reveal several features of the water-vapour distribution over the equatorial Pacific Ocean which has some of the highest sea-surface temperatures (SSTs) in the world. With near-surface relative humidities of about 80%, the longitudinal cross-section is rather uniform and is representative of the mean state of tropical humidity in the marine boundary-layer. However, aloft, there are large differences in relative humidities between longitudes approximately west and east of the date line. At eastern longitudes, the upper troposphere is close to saturation all the way to the tropopause. At western longitudes, a sharp drop in relative humidity to values of 40–50% begins at ~1 km. The humidity decrease is marked by a small, but significant, temperature inversion layer. An example is shown in Fig. 1. The temperature inversion was less pronounced, or absent, at eastern longitudes. Low humidities are maintained until, at an altitude of 6 km, a further drop to values of 10% over ice occurs. In the upper troposphere, above 10–13 km, the relative humidity clearly exceeds 50% on both sides of the date line, despite the extreme dryness east of the date line at lower altitudes. The upper tropospheric values are considerably higher than those previously reported for the tropics (e.g. Rind *et al.* 1991; Sun and Lindzen 1993).

The cross-section of relative humidity derived from the dropsonde releases northward of 3°S for 8 to 21 March is shown in Fig. 9(a). This cross-section spans the longitudes from 160°E to 170°W. Appendix A of Williams (1993) lists details regarding dropsonde location and release dates. While the upsonde flights from the *Vickers* result in a longitudinal as well as a temporal cross-section, Fig. 9(a) represents more or less a longitudinal mean for the period 8–21 March, since the drops collected in Fig. 9(a) were made at times during this period that were not related to any particular longitude. Comparing Fig. 7 with Fig. 9(a), it is evident that both cross-sections are qualitatively similar, given the lower accuracy of the dropsonde-derived humidities. Figure 9(a), too, shows a dry middle troposphere west of the date line and a wet one east of approximately 180°. Since the dropsondes were sampled almost at random with regard to longitude, it is also clear that the humidity cross-section depicted in Figs. 7 and 9(a) represents a stationary pattern and not a temporal trend over the period 8–21 March. However, the stationary pattern can change. This is shown by Fig. 9(b) which depicts the humidity cross-section from dropsonde releases for the period 23 March to 7 April. Now, the dry middle troposphere west of the date line has become wet and, vice versa, the wet upper troposphere east of the date line has turned dry. No valid data from the dropsonde releases exist above 10 km. Thus, it is not known if the switch between wet and dry, and dry and wet, also occurred in the uppermost troposphere. Yet, this seems likely, based on the mirror imaging, that has occurred below 10 km.

(*b*) *Mean profiles*

The humidity profiles from MPI ascents 1–10 (160°E–169°E) and from flights 19–42 (178°E–160°W) were each combined into a mean 'moist' and a mean 'dry' profile. These are shown in Fig. 10(a, b). The moist profile is characterized by relative humidities of around 75% throughout the entire troposphere, except for a small drop to values around 65% from 2 to 4 km. This decrease is a significant feature in the relative-humidity profiles for this part of CEPEX. Caused by contributions of individual wetter and drier profiles, the standard deviation about the mean of the moist profile (Fig. 10(a)) is larger above than below 10 km.

A relative-humidity minimum between 2 and 4 km is also seen in the mean sounding (118 ascents) for the month of February, while the *Vickers* was on station at 156°E for the TOGA/COARE experiment. The mean COARE sounding of relative humidity, together with $\pm 1\ \sigma$ standard deviation, is depicted in Fig. 10(c). Since Humicap-H sensors were

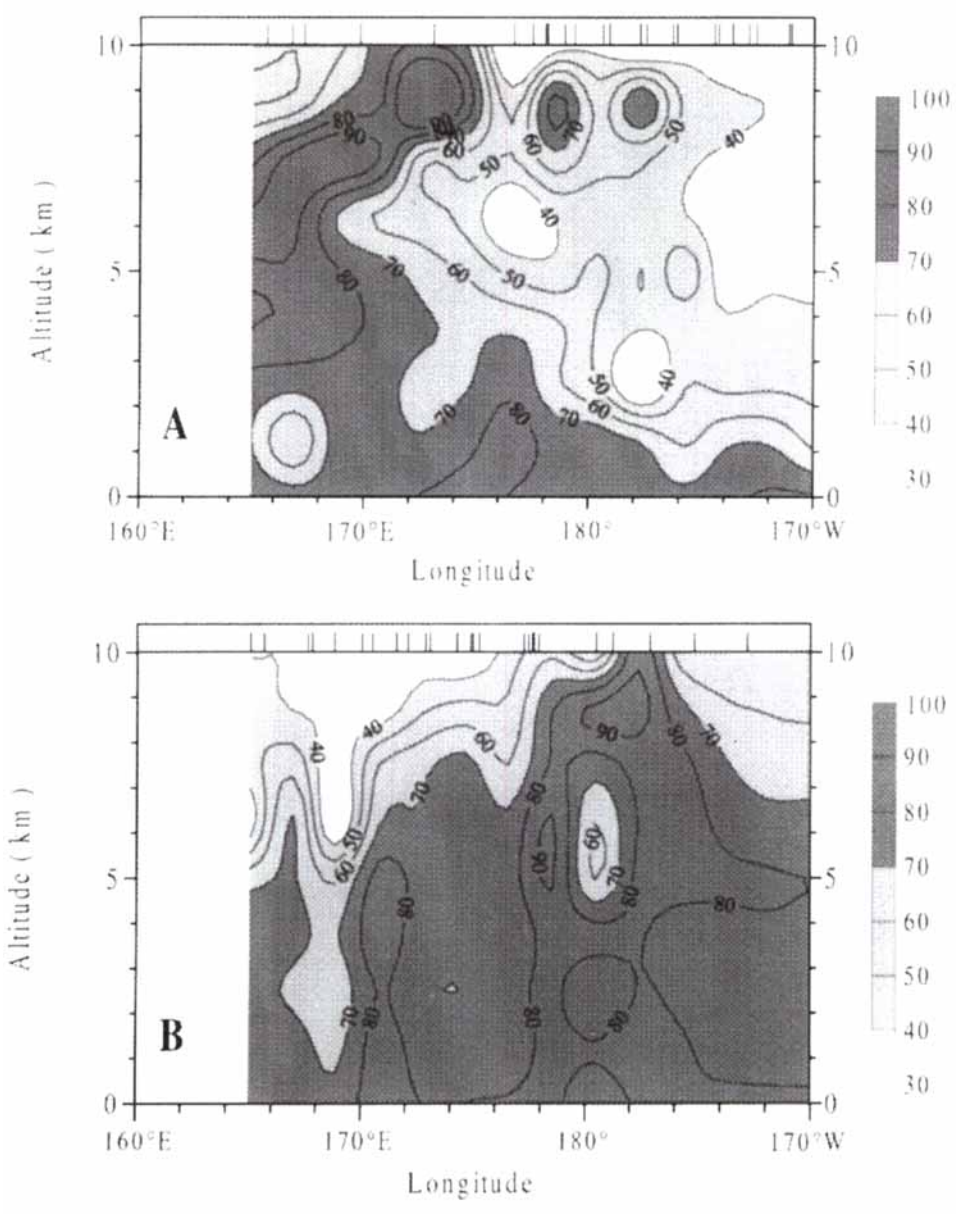

Figure 9. Two-dimensional longitude–altitude cross-section of relative humidity (%) from dropsonde releases northward of 3°S: (a) 8–21 March 1993; (b) 23 March–7 April 1993. Short bars along the top of the diagram indicate longitudes of soundings. Relative humidities are with respect to liquid water for dry temperatures above 273 K and with respect to ice below 273 K.

used, Fig. 10(c) can be directly compared with Fig. 10(a) or (b). The comparison shows that the CEPEX moist profile (Fig. 10(a)) and the mean COARE profile (Fig. 10(c)) are similar within the width of the standard deviation and that the CEPEX dry profile (Fig. 10(b)) is substantially different from the mean COARE profile. Two subsets of the COARE profiles (30 wettest and 30 driest) are plotted in Fig. 10(d) and (e). Evidently, the principal change from the wet to the dry COARE profile is related to the minimum of relative humidity

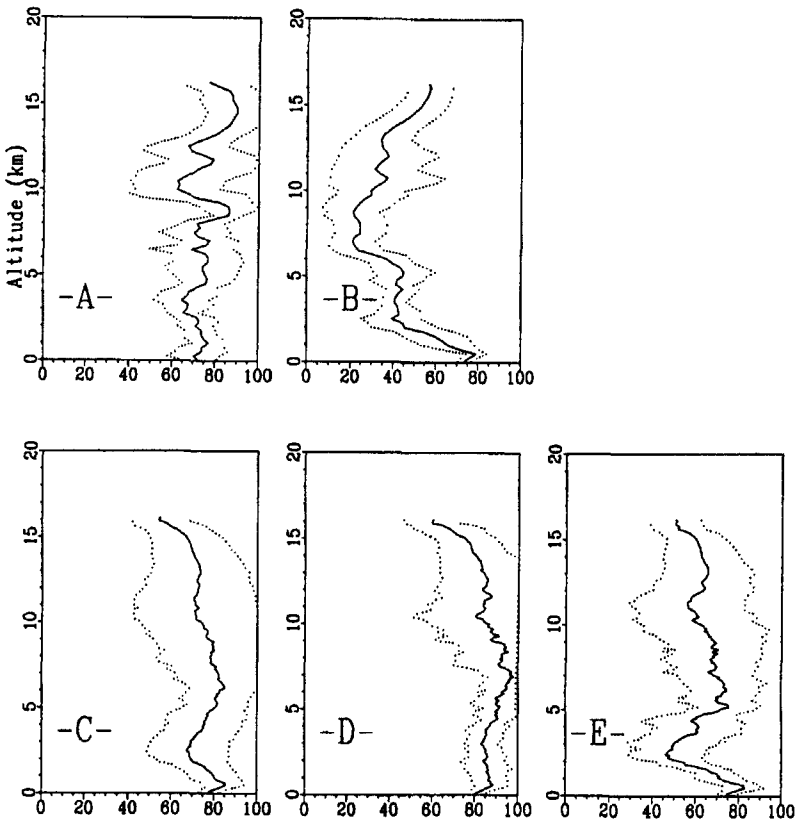

Figure 10. Relative humidity (%) profiles: (a) mean and $\pm 1\sigma$ standard deviation of relative humidity of 'moist' profile (MPI numbers 1–10); (b) mean and $\pm 1\sigma$ standard deviations of relative humidity of 'dry' profile (MPI numbers 19–42); (c) mean humidity profile and $\pm 1\sigma$ standard deviation from 118 COARE soundings during February 1993; (d) mean humidity profile and $\pm 1\sigma$ standard deviation for the 30 wettest soundings out of 118 COARE soundings; (e) mean humidity profile for the 30 driest soundings out of 118 COARE soundings. Relative humidities are with respect to liquid water for dry temperatures above 273 K and with respect to ice below 273 K.

in the low troposphere. This minimum is absent for the wet COARE sounding but more pronounced for the dry COARE sounding. Finally, as for the moist CEPEX profile, the standard deviation about the mean of the COARE profile is larger in the upper than in the lower troposphere.

(*c*) *Relation of humidity profiles to deep and suppressed convection, based on GMS infrared brightness temperature data*

The moist and dry CEPEX profiles can be identified with the presence or absence, respectively, of deep convection. Satellite cloud-top-temperature measurements are available for the spatial and time domain of CEPEX. Satellite radiances in the 10–12 μm spectral window were obtained from the GMS. The radiances were converted to effective black-body temperatures. The black-body temperature (T_b) of optically thick clouds originates from very near cloud top. Hence, $T_b < 250$ K indicates cloud tops at 9 km or higher and, conversely, $T_b > 250$ K can be used as an indicator of the absence of deep convection. A necessary, but not sufficient, condition for deep convection is SST > 300 K (Gadgil

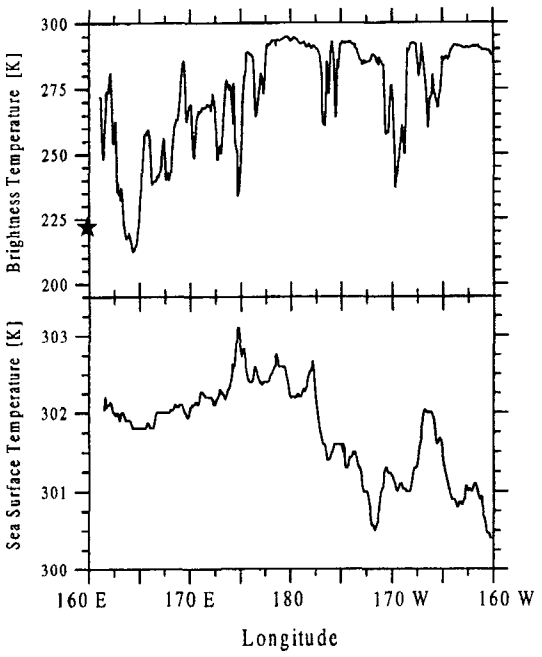

Figure 11. Infrared black-body radiative temperature (K), as derived from GMS data and sea-surface temperatures (K), along the track of the R/V *Vickers*.

et al. 1984; Graham and Barnett 1987). The infrared (IR) black-body radiative temperatures and the sea-surface temperatures for the *Vickers* cruise are displayed in Fig. 11, which shows that conditions conducive to deep convection were encountered at eastern longitudes only. At western longitudes the SST was generally below the chosen threshold, and the IR brightness temperature indicated absence of deep convection, with the possible exception of the longitude near 169°W.

A statistical analysis of the MPI humidity-profiles was performed by sorting the soundings into four categories, according to simultaneously occurring conditions of SST and T_b. These classes are:

class I	SST > 301.5 K and T_b < 250 K	$n = 6$;
class II	SST > 301.5 K and T_b > 250 K	$n = 19$;
class III	SST < 301.5 K and T_b < 250 K	$n = 1$;
class IV	SST < 301.5 K and T_b > 250 K	$n = 14$.

The resulting humidity-profiles and their standard deviations, except the class III profile which contains only one sounding, are shown in Fig. 12(a, b, c). Distinct differences, particularly between class I and class IV profiles, are apparent. Class I conditions, indicating an atmosphere in which recent nearby deep convection is likely, result in a wet profile with relative humidities of about 80%. Class IV, where the relatively low SST and high IR radiation temperature indicate the absence of recent deep convection, shows a humidity profile with surface humidities of 80%, decreasing to 25% at 8 km. Clearly, the means of profiles in class I and class IV are well above and below, respectively, the ensemble mean. Since a powerful criterion is used to classify the humidity profiles according to convection or suppressed convective conditions, and since class I and IV profiles of Fig. 12 are

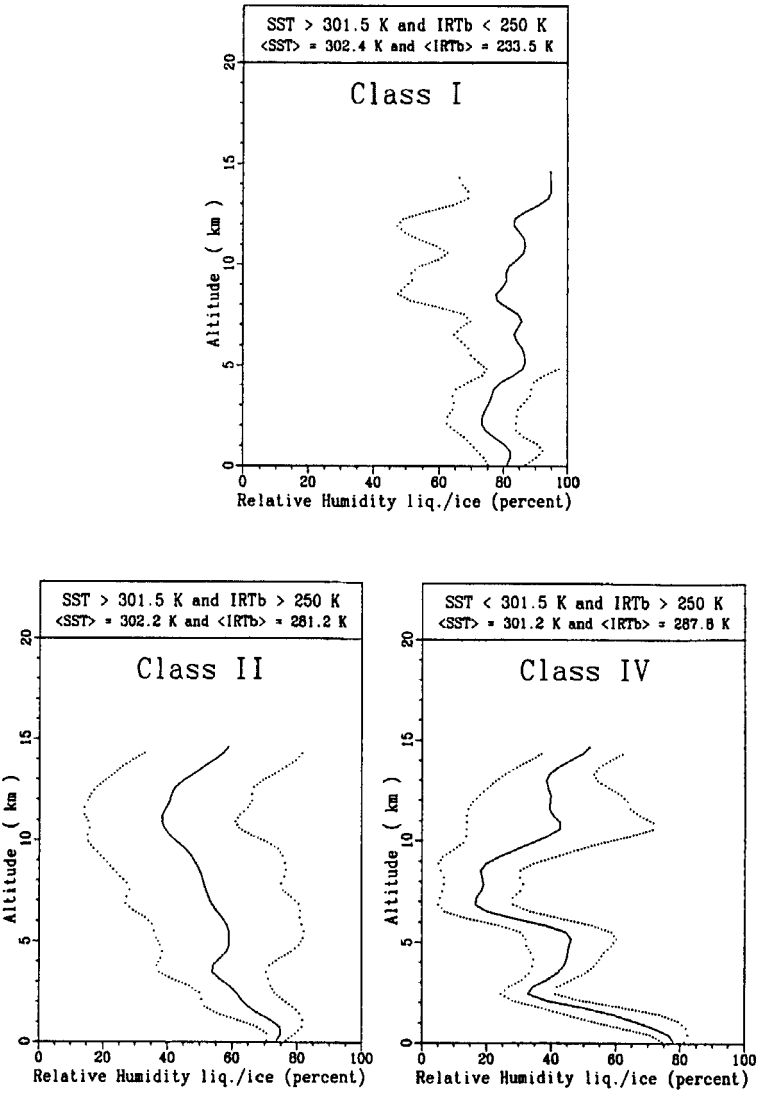

Figure 12. Mean profiles (solid) and standard deviations (dashed) of relative humidity (%) from MPI soundings according to the indicated parameter ranges of SST and infrared cloud-top brightness temperatures (IRTb). (See text.) Relative humidities are with respect to liquid water for dry temperatures above 273 K and with respect to ice below 273 K.

practically identical to the mean wet and dry profiles of Fig. 10 (a) and (b) respectively, it is concluded that

- during the *Vickers* cruise (soundings 1–10) from 160°E–169°E, the atmosphere was under the influence of deep convection. The resulting mean profile of relative humidity was high, close to saturation, with the exception of the altitude range from 2–4 km, where the humidity was significantly lower. The mean COARE water-vapour sounding, obtained at a fixed position of 156°E, was very similar to the class I profile;
- the relative humidity minimum between 2 and 4 km of Fig. 11(a) is not a universal feature of the mean convective profile since the mean of the 30 wettest soundings of

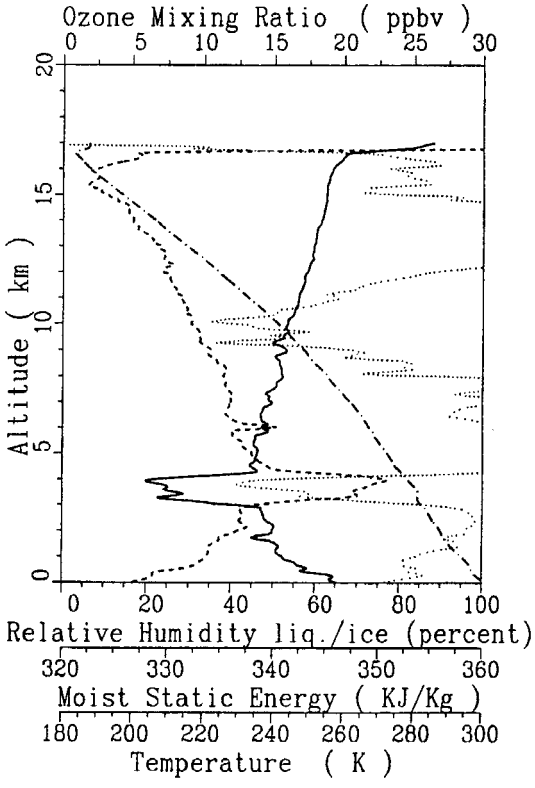

Figure 13. Water and ozone sounding VOF number 1: dry temperature (K) (dashed-dotted); FPH-derived relative humidity (%) (dotted); ozone mixing ratio (parts in 10^9 by volume) (dashed); moist static energy (kJ kg^{-1}) (solid). Relative humidities are with respect to liquid water for dry temperatures above 273 K and with respect to ice below 273 K.

the COARE profiles shows no minimum whereas the relative humidity dips as low as 50% for the mean of the 30 driest COARE soundings;

- a region under the influence of suppressed convection is characterized by low humidity in the middle and upper troposphere;
- above 14 km, even over the convectively suppressed area, the relative humidity over ice was always above 50% but almost certainly below 100%. Four profiles exist over this region that were obtained from frost-point hygrometer measurements (Fig. 6(e, f, g, h)). Only the one taken at 1°59′S, 171°23′W allows saturation within the uncertainty range of the frost-point hygrometer.

5. Ozone profiles and cross-section

Figure 13 shows the vertical ozone-profile from VOF sounding 1 at 9°25′S, 159°58′E, the very first ascent over the convective domain. The simultaneously measured humidity-profile is also shown. The humidity profile is a composite curve from the Humicap A sensor below 5 km and from frost-point hygrometer data above 5 km. A profile of moist static energy Q $(= gz + c_pT + Lq)$ is also shown, where g denotes the acceleration under gravity, z altitude, c_p the specific heat of air, T temperature, L the latent heat of evaporation of water, and q the absolute humidity. The ozone profile of Fig. 13 is unlike anything that has been reported in the literature on tropospheric ozone profiles. The astounding features

of the sounding are the extremely low ozone mixing ratios that were measured in the upper troposphere, with values similar to those near the sea surface. Given the stated accuracy of the ozone measurements, in the upper troposphere near 13 km the profile has an uncertainty which is about equal to the values of the mixing ratios (~5 p.p.b.). However, all three adjacent profiles in the convective region were similar, so that the uncertainty of a composite convective profile would be reduced to about ±3 p.p.b. at 13 km.

The longitudinal cross-section of ozone mixing ratios measured from the soundings of the *Vickers* cruise is presented in Fig. 14. Unfortunately, only three full profiles were obtained in the region that was under the influence of convection. Two more ascents at eastern longitudes reached only 6 km. The ozone cross-section is characterized by the following features:

- mixing ratios near the sea surface are at or below 10 p.p.b. over the whole length of the cruise, from 160°E to 160°W;
- in the middle troposphere (2–4 km) of the convective region a slight but persistent ozone maximum layer of approximately 15 p.p.b. was found;
- the upper troposphere of the convective region has values of ozone mixing ratio which are similar to those near the sea surface;
- the non-convective region (180°–160°W) shows mixing ratios of 20–25 p.p.b. in the middle troposphere, reaching up to the tropopause. However, two pockets of very low mixing ratio (<10 p.p.b.) are located in the upper troposphere, near 170°W and 161°W respectively;
- the vertical gradient of ozone mixing ratio at the tropopause is extremely steep over the convective region;
- over the non-convective region, the ozone gradient is less steep and the ozone mixing ratio does not change much from the middle troposphere to the tropopause.

6. Ozone as a tracer of deep convection

It was mentioned in the introduction that, once an air mass has left the marine boundary-layer in a forced cumulonimbus (Cb) ascent, the chemical lifetime of ozone in it becomes long. Mixing ratios of ozone at the tropopause as low as those near the surface are understandable if air from the subcloud layer is lifted all the way to the tropopause in the inner core of undiluted Cb convection. The equivalence of surface and top-of-the-troposphere ozone mixing ratios, plus the steepness of the ozone gradient which starts at the tropopause, together form an excellent indicator of the nature and the intensity of the transfer process. Depending on season and SST, the bulk of the lateral Cb outflow is centred between 300 and 200 hPa (Riehl and Simpson 1979). However, a considerable fraction can reach even higher levels. The tropopause is the ultimate limit, except for the possibility of overshooting above the static equilibrium level. The extreme steepness of the ozone gradient, at the tropopause, is a powerful indicator that Cb convection has reached the top of the troposphere and, conversely, that no ozone from the stratosphere was able to diffuse into even the uppermost layers of the troposphere. The latter can happen if an upward-directed mass-flow exists at the tropopause and counteracts downward diffusion. While the implications for exchange between the troposphere and stratosphere were discussed by Vömel *et al.* (1995b), it is evident from these CEPEX observations that deep convection, during the active phase, effectively makes the tropopause an impermeable surface which prevents stratospheric ozone from penetrating into the troposphere.

Thus, the observations suggest that the absence, or near-absence, of ozone in the upper troposphere may be used to diagnose recent deep convection. This tool would be

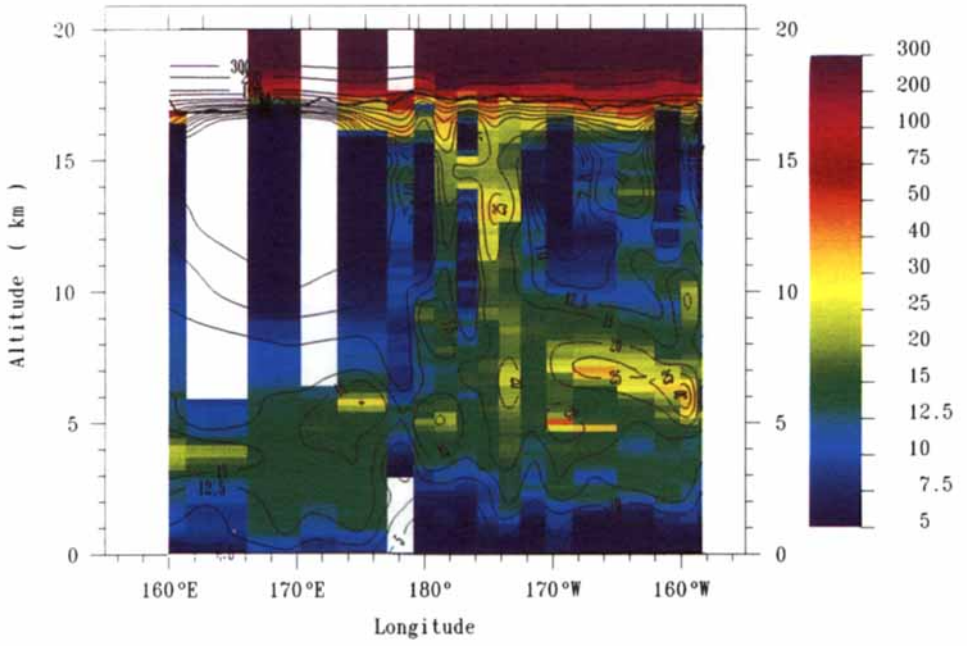

Figure 14. Two-dimensional longitude–altitude cross-section of ozone mixing ratio (parts in 10^9 by volume) from the R/V *Vickers* cruise along 2°S, 160°E to 160°W, 7–19 March 1993. Short bars along the top of the diagram indicate longitudes of soundings. The black line indicates location of the tropopause.

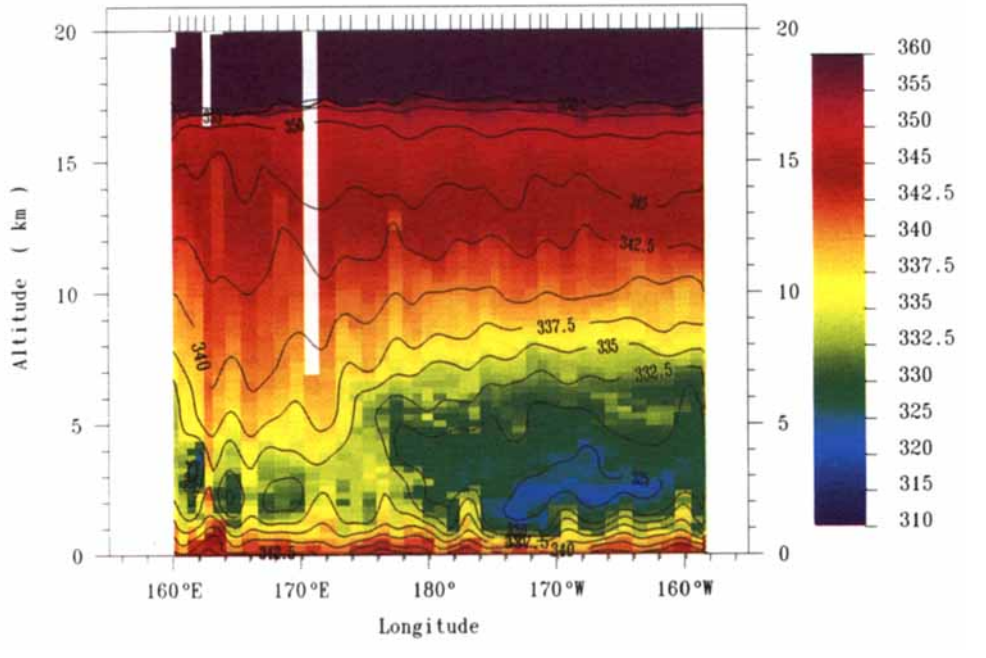

Figure 15. Two-dimensional longitude–altitude cross-section of moist static energy $Q = gz + c_pT + Lq$ (kJ kg^{-1}) during the R/V *Vickers* cruise. Short bars along the top of the diagram indicate longitudes of soundings. The black line indicates location of the tropopause.

independent of the conventional ones, such as highly-reflective-cloud index, cloud-top height or cloud-top radiative temperature, which are all based on the water substance. There are two ways to proceed from here. Firstly, one might argue that this diagnostic tool might be validated, using experimental observations and conventional diagnostic tools. This line of argument, however, results in circular reasoning unless enough observations are collected to allow them to be evaluated statistically. So, in the absence of a statistically valid data-base, a second approach is taken: the ozone diagnostic tool will be used as it stands and applied to the water-vapour observations. This will be done in section 8.

First, however, it is necessary to discuss the origin of the ozone which is observed in the middle troposphere of the convective CEPEX domain.

On the arguments used so far, the entire troposphere, at all heights over the deep convective domain of the CEPEX area, might be expected to be devoid of ozone—not just the bottom and top layers. Consequently, it is surprising to see, in Fig. 14, that the ozone mixing ratio in the middle troposphere, between heights of approximately 2 km and 6 km, has values near 20 p.p.b.v. Although this is low in absolute terms, it is nevertheless substantially higher than the values in the subcloud layer or those in the upper troposphere.

How can the enhanced ozone mixing ratios in the middle troposphere of the convective region be explained? A likely scenario is as follows. In non-convective regions of the troposphere, stratospheric ozone intrudes into the troposphere, presumably by eddy mixing across the tropopause, maybe compensating for some overshooting or general upward flow in the convective regions. This would provide a certain downward ozone-flux at the top of the troposphere. In fact, except for two pockets of very low ozone mixing ratio in the upper troposphere east of the date line, the free troposphere of that region shows nearly constant ozone mixing ratios of 20–25 p.p.b. which indicates that convection there had not recently occurred. The GMS brightness data show that, during this section of the *Vickers* cruise, the area was cloud free. Therefore, estimates of subsidence can be made by equating diabatic warming $-wS$ to the radiative cooling rate. The static stability $S = T\theta^{-1}(\partial\theta/\partial z)$ was calculated from the sounding data. Values of S ranged from +1 to +2 K km^{-1} above 10 km altitude, to values around 3–4 K km^{-1} below 10 km. The cooling rate was estimated at $\sim$1 K d^{-1} (Inamdar, personal communication). These cooling rates are lower than the usual 2 K d^{-1} (Dopplick 1972). This estimate results in a downward velocity of $w \approx -1$ km d^{-1} above 10 km. Strong subsidence is clearly demonstrated by the very dry troposphere over the convectively suppressed troposphere (Fig. 7).

Now, assume that convection starts: ozone-deficient air is lifted from the subcloud layer, bypasses the middle troposphere, and is expelled over the height range that the convection reaches. This process would, depending on the intensity, extent and frequency of the convection events, generate a vertical distribution of ozone similar to what is observed. After the Cb convection ceases, the upper troposphere would again attain the undisturbed steady-state distribution. However, if the convection is assumed to prevail over a large area, say that of a synoptic disturbance, then the middle troposphere would lose its ozone content as ozone descended into the subcloud layer and was destroyed there. In fact, much of the ozone in the whole region is probably imported, since ozone is destroyed everywhere because of a lack of NO_x sources. Thus, a source of ozone is required which is outside the convective region and yet supplies ozone to the middle troposphere within it. Since radiative cooling of clear air causes transport into convective regions from non-convective regions to slope downwards, the source of the ozone in the middle troposphere of the convective region must be the upper troposphere, or even the stratosphere, of non-convective regions.

This assertion, which needs to be substantiated by trajectory analyses, has consequences for the process of maintaining convection because the long-range, sloping, lateral transport advects dry air into the convective region. This is seen in Fig. 13 which clearly

supports the assertion. Figure 13 shows that the lateral, sloping transport of dry, relatively ozone-rich, air to the convective region occurs in a narrow, stream-like layer. Since Fig. 13 is one of several examples and, furthermore, since the mean convective CEPEX sounding (Fig. 10(a)) as well as the mean COARE sounding (Fig. 10(c)) all show a layer of low humidity near 700 hPa, it is concluded that long-range transport and large-scale dynamics can play a significant role in regulating deep convection over the warm oceans. In essence, we are speculating that there is a strong linkage between large-scale dynamics and deep convection. The role of deep convection in driving the large-scale circulation (through latent-heat release) is well known. What is not known, however, is whether dry air transported by the large-scale circulation can regulate deep convection. The present results suggest that the well-known minimum of moist static energy (or of equivalent potential energy) at about 700 hPa may be a result of this linkage. If this is so, then, a negative feedback to deep convection seems to operate, so that advection and entrainment of dry air acts like a controlling valve (low Q or θ_e) which regulates free convection.

The cross-section of moist static energy for the *Vickers* cruise is shown in Fig. 15. Clearly, the minimum of Q is much less pronounced in the most convective region. The 30 wettest soundings at 156°E (Fig. 10(d)) do not reveal a layer of minimum humidity. The mean profile of Q for these soundings is almost constant with altitude. Unfortunately, no ozone soundings exist for the COARE series, so that long-range transport from non-convective areas to 156°E cannot be demonstrated through the anticorrelation between ozone and water vapour.

The CEPEX results at least suggest that there is long-range, sloping, transport of low-humidity air into the convective region. In the two-dimensional view of Fig. 14, the 20–25 p.p.b. isopleths of ozone mixing ratio are connected to the uppermost levels of the troposphere near 175°W. The meridional wind velocities (Fig. 16) were rather small, indicating the possibility that the transported air-masses originated close to the plane of the figure, i.e. in equatorial latitudes. It is interesting to note that the zonal wind velocity (Fig. 17) was strongly divergent in the tropopause region near 170–175°W. This is an indication of downward transport at these longitudes.

7. Source of low values of ozone mixing ratio in the upper troposphere of the convectively suppressed region

Figure 7 demonstrates that high humidity (>50% with respect to ice) was prevalent in the upper troposphere, including the convectively suppressed CEPEX domain. Comparing Fig. 7 and Fig. 14, it is apparent that two 'pockets' of high humidity, in the upper troposphere near 170°W and 160°W, are correlated with very low values of the ozone mixing ratio. A convective origin for these pockets is indicated. Selecting the longitude near 171°W which the *Vickers* passed on 15 March, Fig. 18 shows the GMS IR brightness temperatures for this location, backward in time from 0600 GMT 5 March. It is apparent that convection had been absent from the area for the previous ten days. Consequently, upper tropospheric outflow from other convective areas elsewhere must be involved. Figure 16 demonstrates that the low-ozone–high-humidity pockets had a southerly origin. Strong (15 m s^{-1}) winds had advected air masses over more than 10° of latitude in a day. The CEPEX operations summary (Williams 1993) shows daily 200 hPa analyses from the European Centre for Medium-Range Weather Forecasts (ECMWF). A simple isobaric trajectory analysis identifies the upper tropospheric outflow of the tropical cyclone *Roger* and an active band of deep convection which extended from *Roger* (16°S, 156°E) across Fiji and then south-eastwards as the likely source of low-ozone–high-humidity in the upper troposphere at 171°W.

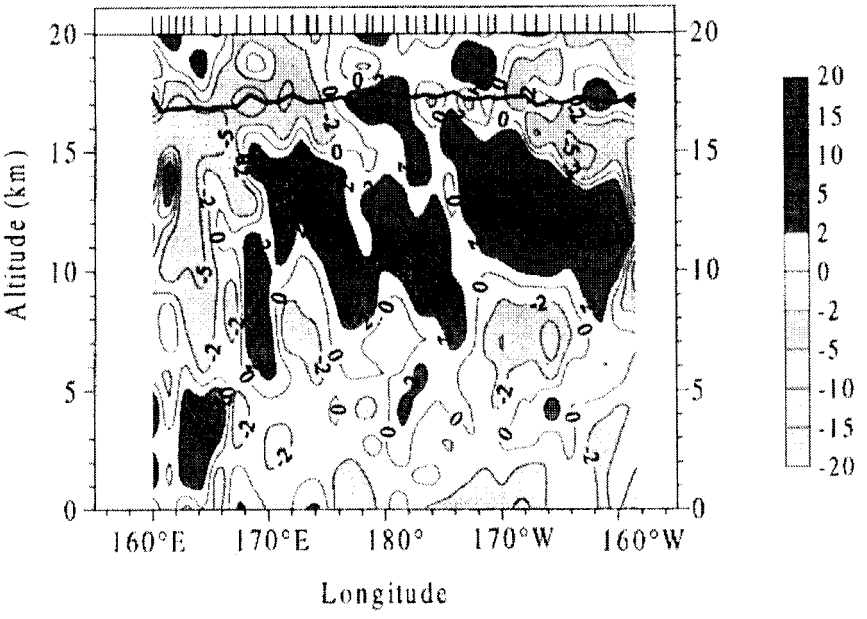

Figure 16. v-component of wind speed (m s^{-1}) from MPI radiosonde releases during the R/V *Vickers* cruise. Short bars along the top of the diagram indicate longitudes of soundings. The black line indicates location of the tropopause.

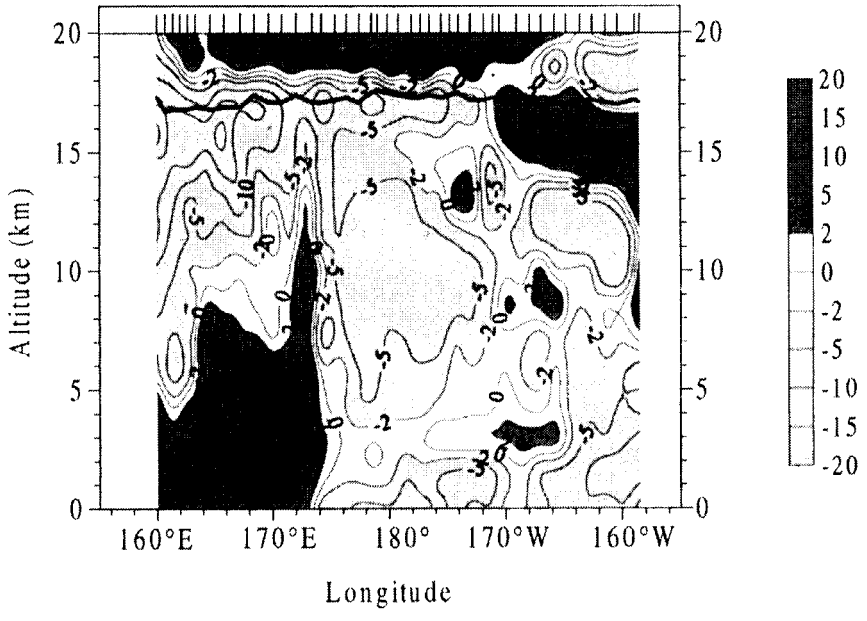

Figure 17. u-component of wind speed (m s^{-1}) from MPI radiosonde releases during the R/V *Vickers* cruise. Short bars along the top of the diagram indicate longitudes of soundings. The black line indicates location of the tropopause.

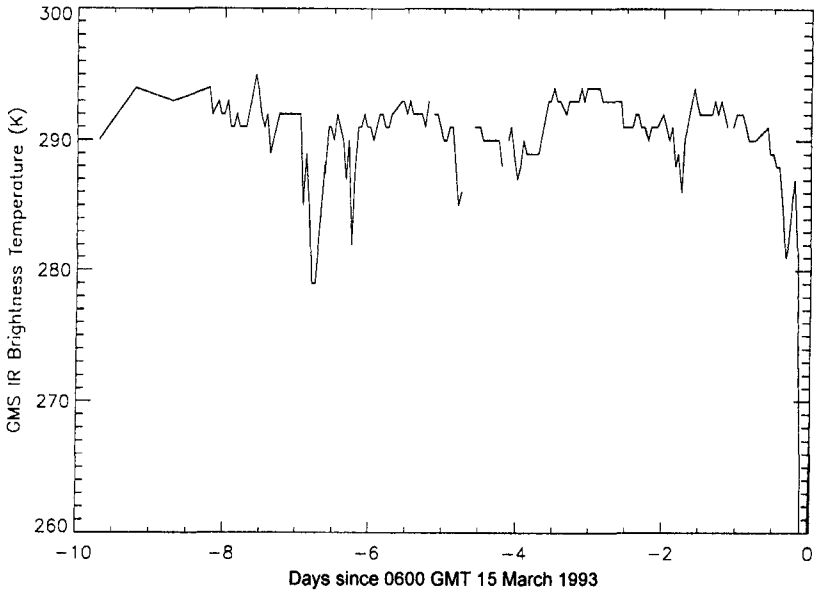

Figure 18. GMS infrared brightness temperatures (K) at 170°30′W at 0600 GMT 15 March and for 10 days backwards in time.

Consequently, using the absence, or near-absence, of ozone in the upper tropical troposphere as a tool to diagnose deep convection does not allow us to conclude that transport from the marine boundary-layer was strictly vertical. Indeed, if we treat the mixing ratio of ozone as a conservative quantity, this result implies that air which ascends during deep convection can subsequently be advected, free of divergence, for a considerable distance from the outflow region. The advective transport in this example was probably close to isobaric, since the relative humidity still exceeded 50%.

8. Relative humidity in the deep convective troposphere

It is clear that, in an ascending hot tower of Cb convection, the relative humidity (with respect to ice when $T < 273$ K and to water when $T > 273$ K) should be very close to 100%. However, the fractional area of active deep convection is rather small, of the order of 0.001 of the area of the equatorial-trough zone (Riehl and Simpson 1979). Since radiosonde balloons rarely survive a hot-tower ascent, Figs. 10(a, c) and 12(a) are representative of the humidity profile for the tropical troposphere under the influence of convection.

The air outside the undiluted towers of deep convection is known to subside, for reasons of mass continuity. This also enhances positive buoyancy inside the towers. At first sight, then, it is surprising to observe high relative humidity in the convectively modified troposphere. Given the measured temperature lapse rate of 8–9 K km^{-1}, and assuming 100% humidity with respect to ice at the base of Cb anvils, it is not possible to retain high humidity in the subsiding air (because a descent of only about 1 km is enough to reduce the relative humidity to 50%). Further descent leads to a very dry troposphere. Consequently, the CEPEX observations imply that there must be a source of humidity in the subsiding air.

This point was also made by Sun and Lindzen (1993). They argued that the source of humidity in the subsiding air has to be the evaporation of water in upper-level clouds as moistened air mixes with drier air, and the evaporation of hydrometeors falling from the

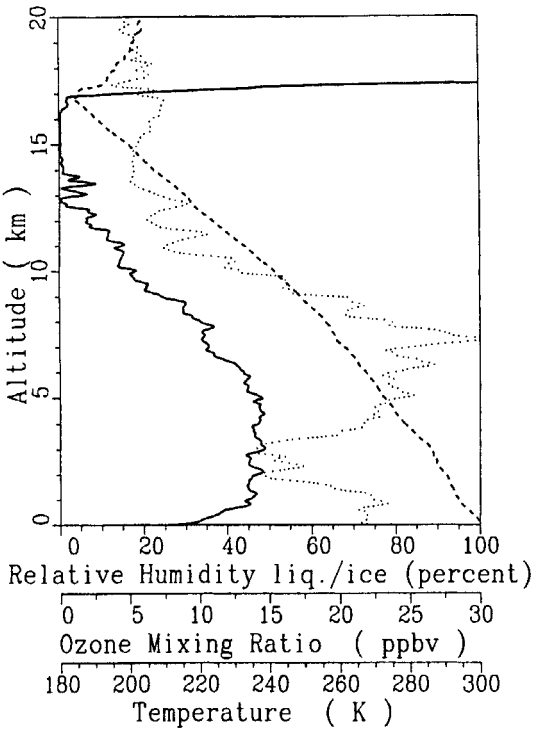

Figure 19. Profiles for 9 March 1993: ozone mixing ratio (parts in 10^9 by volume) from VO sounding 3, made 2259 GMT at 2°01′S, 169°35′E (solid); relative humidity (%) from MPI sounding 11, made 2358 GMT at 2°03′S, 169°41′E (dotted); temperature (K) from MPI sounding 11 (dashed line). Relative humidities are with respect to liquid water for dry temperatures above 273 K and with respect to ice below 273 K.

base of the anvils. Using a heuristic model of deep convection, they argued that the time constants for evaporation of ice crystals were long compared with their fall velocity, so that there would not be appreciable moistening of the subsiding air. Their model predicts a dry tropical troposphere. However, they used conventional, non-validated, radiosonde data for the adjustment of their model parametrization.

In the present paper, we have used calibrated radiosonde results and GMS IR brightness temperatures to show that the convective atmosphere is moist (and, indeed, close to saturation). However, since the diagnosis of convection is based on the presence of cloud above 9 km, this result applies only to the timescale during which the anvil has not dissipated and to the spatial scale that is covered by the anvil.

The use of low values of upper-tropospheric ozone mixing ratio as a tool for diagnosing deep convection does not depend on water in any of its three phases and is, therefore, applicable also to cloud-free air, to areas with subsidence or to longer timescales.

Ozone sounding number 3, at 169°35′E, is shown in Fig. 19, along with the corresponding temperature profile: on the basis of the ozone-based criteria for deep convection given in section 6, it is a deep convective sounding. Indeed, it is our best example, showing the steepest ozone gradient, exactly at the tropopause, and the lowest upper-tropospheric ozone mixing ratios. Yet, the GMS-brightness-temperature test fails and, furthermore, MPI humidity-profile number 11, taken at 169°41′E, shows a dry troposphere above 8 km.

Figure 20 presents a time sequence of GMS brightness temperatures over the area, with a cross marking the position of the R/V *Vickers*, at the time of MPI sounding number 11. Panel (a) shows the brightness temperature two hours after the MPI sounding;

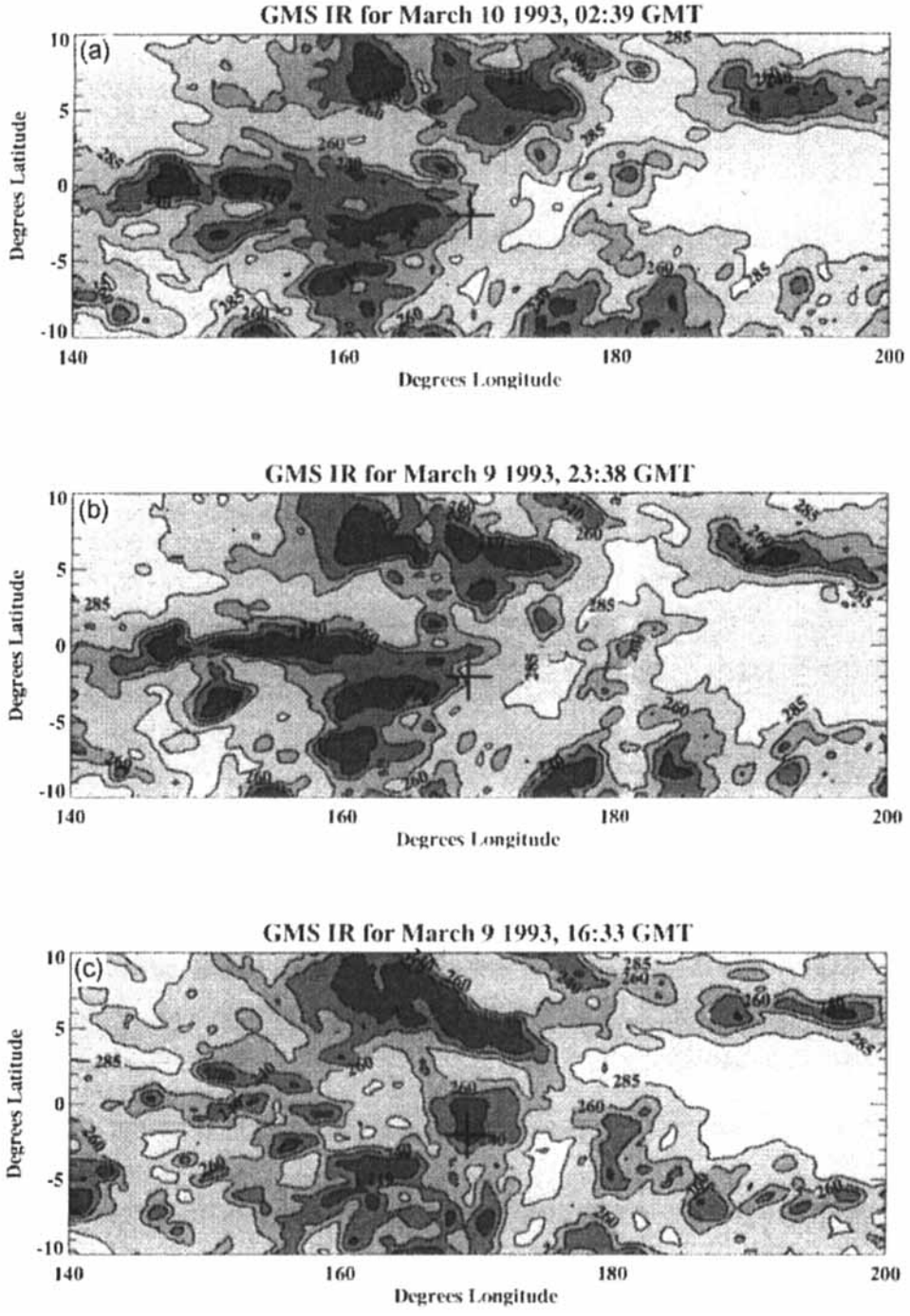

Figure 20. GMS infrared brightness temperature (K): (a) 2 hours after MPI sounding 11; (b) at the time of MPI sounding 11; (c) 7 hours before MPI sounding 11. The position of the R/V *Vickers* at the time of MPI sounding 11 is indicated by a cross.

(b) represents the brightness temperature at the time of the sounding and (c) the temperature field 7 hours before the sounding.

Figure 20 demonstrates that, 7 hours before the sounding was made, deep convection was active at 169°41′E (since the IR brightness temperature was <220K). At $t - 4$ hours (not shown in Fig. 20) the conditions were similar. At the time of the sounding $t = 0$, deep convection had moved to the west. Brightness temperatures of 260 K at the location of the sounding reveal a clear upper atmosphere. Figure 19 shows that 100% humidity, i.e. cloud, was measured at a height of 7 km , exactly at $T = 260$ K. As Fig. 20(a) indicates, two hours after the sounding the IR brightness temperature had not changed; however, on the large scale, the convection was moving farther westwards.

Whereas the ozone sounding (Fig. 19) reveals a convective origin of the upper tropospheric air, the GMS sequence (Fig. 20) implies that the drying of the upper troposphere, depicted in Fig. 19, happened within seven hours, or less, of the cessation of active convection over the target area. Given the measured wind velocity, advection from roughly 1° of longitude to the east could possibly have transported air to the location of the sounding during the seven hours. However, Fig. 20 shows that, seven hours before the sounding, there was active convection over 4° of longitude upwind. This suggests that moistening by advection may not be the process that is principally responsible for the water supply to the upper atmosphere and, conversely, that the dominant mechanism is evaporation of precipitation. Drying starts when the supply of hydrometeors, falling out of the anvil, has stopped. Figure 8 shows that, between 10 and 15 km, the humidity mixing ratio at 169°41′E was about half that at the same height in adjacent soundings. Thus, low relative humidity and lower mixing ratios substantiate the subsidence assertion. As soon as the anvil has dissipated, and precipitation has reached the low troposphere or ground, drying sets in, caused by subsidence. This process will lower the relative humidity and, in comparison with water-vapour mixing ratios at the same height in adjacent non-subsiding areas, mixing ratios will also be lower.

Further, since active convection and a moist tropical troposphere are closely coupled, a logical corollary of the above seems to be that the moisture content of the tropical troposphere is related to the frequency and spatial extent of deep convection. This would also explain the observation (e.g. Stephens 1990; Inamdar and Ramanathan 1994) that time averages show a very humid atmosphere over warm pools. The reason seems to be that the frequency of convection (as shown convincingly by Zhang (1993)), and the residence time of water vapour in the tropical atmosphere (in view of the above), both increase with SST.

9. Conclusions

Calibrated humidity sensors were flown on radiosonde balloons and dropped from high-flying aircraft during the Central Equatorial Pacific Experiment (CEPEX) and the Coupled Ocean–Atmosphere Response Experiment (COARE).

The resulting profiles of relative humidity and mixing ratio have been classified, according to whether convection was deep or suppressed. Independently, active deep convection was diagnosed by satellite measurements of IR black-body cloud-top radiative temperature. In active deep convection, the tropical troposphere was found to have high values of relative humidity up to the tropopause, close to 80%, over liquid or ice as appropriate.

Between heights of 2 to 4 km (~700 hPa), however, the atmosphere was found, on average, to be drier, with relative humidities of around 65 to 70%. Correlations of relative humidity with quasi-simultaneously measured mixing ratios of ozone were negative,

implying that drier air at 700 hPa in the convective atmosphere originated in the upper troposphere of non-convective regions. The minimum of moist static energy near 700 hPa in the tropical troposphere may have been the result of long-range advection of dry air and, furthermore, this transport may have played an important role in regulating deep convection.

The near-absence of ozone in the uppermost levels of the tropical troposphere was used as a quasi-conservative tracer of recent deep convection. This allowed the evolution of relative humidity, and of mixing ratio, to be followed to times after the dissipation of the cloud anvil, when the GMS-based diagnosis of deep convection was no longer applicable. Within hours of anvil dissipation, the troposphere was dry above 8 km, and the mixing ratio was low. The drying was achieved through subsidence in clear air. Consideration of the drying timescale, suggests that evaporation of precipitation, falling out from the cloud anvil, was the moisture source of the troposphere during active convection, i.e. at times when the cloud anvil was still optically thick.

Acknowledgements

CEPEX was funded by the U.S. National Science Foundation and the U.S. Department of Energy. The paper constitutes publication number 149 of the Center for Clouds, Chemistry and Climate, Scripps Institution of Oceanography, La Jolla, California, USA.

References

Antikainen, V. and Paukkunen, A. 1994 'Studies on improving humidity measurements in radiosondes'. Pp. 137–141 in *Instruments and observing methods*, Report No. 57, WMO-TD-No. 588. World Meteorological Organization, Geneva

Burnett, C., Carli, B., DeMore, W. B., deZafra, R., Evans, W. F. J., Guthry, P. D., Hampson, R. F., Heaps, W., Jones, R., Kley, D., Prather, M., Russell, J. M. III, Schmidt, U., Traub, W. A. and Watson, R. T. 1985 'Hydrogen species'. Pp. 456–476 in *Atmospheric Ozone*, Global Ozone Research and Monitoring Project, Report No. 16. World Meteorological Organization, Geneva

CEPEX 1993 *Central Equatorial Pacific Experiment. Experiment Design.* Center for Clouds, Chemistry and Climate (C^4), a National Science Foundation Science and Technology Center, at Scripps Institution of Oceanography at the University of California, San Diego, USA

Cole, H. 1993a 'The TOGA COARE ISS radiosonde temperature and humidity errors'. Technical Report, National Center for Atmospheric Research, Boulder, Colorado, USA

1993b 'The heated carbon humidity sensor for use in CEPEX'. Status Report, Surface and Sounding Systems Facility, National Center for Atmospheric Research, Boulder, Colorado, USA

Crutzen, P. J. 1973 A discussion of the chemistry of some minor constituents in the stratosphere and troposphere. *Pure Appl. Geophys.*, **106–108,** 1385–1399

Dopplick, T. G. 1972 Radiative heating for the global atmosphere. *J. Atmos. Sci.*, **29,** 1278–1294

Gadgil, S. P., Joseph, P. U. and Joshi, N. U. 1984 Ocean–atmosphere coupling over monsoon regions. *Nature*, **312,** 141–143

Graham, N. E. and Barnett, T. P. 1987 Sea surface temperature, surface wind divergence and convection over tropical oceans. *Science*, **238,** 657–659

Inamdar, A. and Ramanathan, V. 1994 Physics of greenhouse effect and convection in warm oceans. *J. Climate*, **7,** 715–731

Johnson, J. E., Gammon, R. H., Larsen, J., Bates, T. S., Oltmans, S. J. and Farmer, J. C. 1990 Ozone in the marine boundary-layer over the Pacific and Indian Oceans: latitudinal gradients and diurnal cycles. *J. Geophys. Res.*, **95,** 11842–11856

Kley, D. and Stone, E. J. 1978 Measurement of water vapour in the stratosphere by photodissociation with Ly-α (1216Å) light. *Rev. Sci. Instrum.*, **49,** 691–697

Liu, S. C., McFarland, M., Kley, D., Zafiriou, O. and Huebert, B. 1983 Tropospheric NO_x and O_3 budgets in the equatorial Pacific. *J. Geophys. Res.*, **88,** 1360–1368

Mastenbrook, H. J. 1966 'Water vapour observations at low, middle and high latitudes'. NRL Report 6447, Naval Research Laboratory, Washington, DC, USA

1968 Water vapour distribution in the stratosphere and high troposphere. *J. Atmos. Sci.*, **25,** 299–311

Mastenbrook, H. J. and Oltmans, S. J. 1983 Stratospheric water vapour variability for Washington, DC/Boulder, CO: 1964–82. *J. Atmos. Sci.*, **40,** 2157–2165

McFarland, M., Kley, D., Drummond, J. W., Schmeltekopf, A. L. and Winkler, R. H. 1979 Nitric oxide measurements in the equatorial Pacific region. *Geophys. Res. Lett.*, **6,** 605–608

Piotrowicz, S. R., Borau, D. A. and Fischer, C. K. 1986 Ozone in the boundary layer of the equatorial Pacific Ocean. *J. Geophys. Res.*, **91,** 13113–13119

Piotrowicz, S. R., Bezdek, H. F., Harvey, G. R., Springer-Young, M. and Hanson, K. J. 1991 On the ozone minimum over the equatorial Pacific Ocean. *J. Geophys. Res.*, **96,** 18679–18687

Riehl, H. and Malkus, J. S. 1958 On the heat balance in the equatorial trough zone. *Geophysica (Helsinki)*, **6,** 503–538

Riehl, H. and Simpson, J. 1979 The heat balance of the equatorial trough zone revisited. *Contr. Atmos Phys.*, **52,** 287–306

Rind, D. E., Chiou, W., Chu, W., Larsen, J., Oltman, S. S. J., Lerner, J., McCormick, M. P. and McMaster, L. 1991 Positive water vapour feedback in climate models confirmed by satellite data. *Nature*, **349,** 500–503

Smit, H. G. J., Sträter, W., Kley, D. and Proffitt, M. H. 1994 'The evaluation of ECC ozone-sondes under quasi flight conditions in the environmental chamber at Jülich'. In *Transport and transformation of pollutants in the troposphere*. P.M. Borrell, P. Borrell, T. Cvitas and W. Seiler (eds.), SPB Academic Publishing, The Hague, Netherlands

Stephens, G. L. 1990 The relationship between water vapour over the oceans and sea surface temperature. *J. Climate*, **3,** 634–635

Sun, D.-Z. and Lindzen, R. S. 1993 Distribution of tropical tropospheric water vapour. *J. Atmos. Sci.*, **50,** 1643–1660

Thompson, A. M., Johnson, J. E., Torres, A. L., Bates, T. S., Kelly, K. C., Atlas, E., Greenberg, J. P., Ponahne, N. M., Yvon, S. A., Saltzman, E. S., Heikes, B. G., Mosher, B. W., Shashkov, A. A. and Yegorov, V. I. 1993 Ozone observations and a model of marine boundary-layer photochemistry during SAGA 3. *J. Geophys. Res.*, **98,** 16955–16968

Torres, A. L. and Thompson, A. M. 1993 Nitric oxide in the equatorial Pacific boundary-layer. *J. Geophys. Res.*, **98,** 16949–16954

Väisälä 1991 Information Release SR 0559. Väisälä Oy, SF 00Y21, Helsinki, Finland

Vömel, H., Oltmans, S. J., Hofman, D. J., Deshler, T. and Rosen, J. H. 1995a The evolution of the dehydration in the Antarctic stratospheric vortex. *J. Geophys. Res.*, **100,** 13919–13926

Vömel, H., Oltmans, S. J., Kley, D. and Crutzen, P. J. 1995b New evidence for the stratospheric dehydration mechanism in the equatorial Pacific. *Geophys. Res. Lett.*, **22,** 3235–3238

Webster, P. J. and Lukas, R. 1993 TOGA-COARE: The coupled ocean–atmosphere response experiment. *Bull. Am. Meteorol. Soc.*, **73,** 1377–1416

Williams, S. F. 1993 *Central Equatorial Pacific Experiment (CEPEX), Daily operations Summary*. University Cooperation for Atmospheric Research, Office of field project support. Boulder, Colorado, USA

Zhang, C. 1993 Large-scale variability of atmospheric deep convection in relation to sea surface temperature in the tropics. *J. Climate*, **6,** 1898–1913